Cadherin-mediated cell-cell adhesion regulates collective pediatric glioma cell migration

Dayoung Kim[1], James M Olson[2,3] and Jonathan A Cooper[1]*

1 Basic Sciences Division, Fred Hutchinson Cancer Center, Seattle, WA, 98109, USA

2 Clinical Division, Fred Hutchinson Cancer Center, Seattle, WA, 98109, USA

3 Ben Towne Center for Childhood Cancer Research, Seattle Children's Research Institute, Seattle, WA, 98101, USA

Abstract

Pediatric high-grade gliomas are highly invasive and cure rates are low. Tumor cells invade along varied migratory tracks, following neural cell strands or extracellular matrix around blood vessels, resembling neuron progenitors during brain development. In contrast to their adult counterparts, mechanisms that direct invading cells to follow these different routes remain poorly characterized. We found that N-cadherin differentially regulates pediatric high-grade glioma collective migration according to the microenvironment, inhibiting invasion of extracellular matrix but stimulating migration on neurons or astrocytes. Migrating leader cells exhibited faster endocytosis of N-cadherin and β-catenin and increased proliferation and nuclear Yes-associated protein 1 (YAP1) relative to follower cells. YAP1 localization was regulated by cell density, and inhibition of YAP1 and its paralog TAZ decreased N-cadherin internalization and retarded migration. Therefore, feedback between YAP1/TAZ and N-cadherin recycling regulates leader-follower phenotypic identity and differential migration on extracellular matrix and neural substrates.

Keywords pediatric brain tumor, pediatric high-grade glioma, cell-cell adhesion, collective migration, leader cell, endocytosis, N-cadherin, YAP1

*Correspondence: jcooper@fredhutch.org

Introduction

Pediatric high-grade gliomas (PHGGs) and diffuse midline gliomas (DMGs) are highly invasive, making them both impossible to surgically remove and challenging to effectively treat with available therapies [1]. Invasion occurs along a variety of routes, including between neural cells in the gray matter, along axon tracts in the white matter, and along extracellular matrix (ECM) under the leptomeninges and in the perivascular niche [2-7]. These invasion routes and morphologies of migrating glioma cells resemble those of migrating neural progenitors and immature neurons during brain development, suggesting that similar molecular mechanisms may be at play [4,8-10]. A single tumor xenograft exhibits phenotypic plasticity and can invade the surrounding tissue by slow, directed, collective migration or fast, random, individual cell migration [6]. Molecular and phenotypic profiling reveals multiple tumor subclones with distinct invasive capacity that cooperate in vitro [11], but the molecular and cellular mechanisms contributing to invasion in different microenvironments are poorly understood.

The ability of glioma cells to migrate either between other cells or through ECM implies differential regulation of cell-cell and cell-matrix interactions [12]. Adhesions between glioma cells may allow them to coordinate their movements during collective migration, while adhesions between glioma cells and normal cells may aid invasion into host tissue and loss of cell-cell adhesions increases single-cell migration [13-16]. The plasticity between individual and collective migration implies that adult glioma cells can adapt to making contacts with normal cells or with other tumor cells, but the specific molecules involved are unknown.

Homotypic cell-cell adhesions are commonly made by classic cadherins. N-cadherin (*CDH2*, N-cad) is abundantly expressed in the developing brain and critical both to stabilize the neuroepithelium and for migration of neural progenitors and neural crest cells [17-25]. At the molecular level, N-cad is a transmembrane protein, making homophilic interactions with N-cad on neighboring cells that can promote cell-cell adhesions or can stimulate contact inhibition of locomotion, in which transient cell-cell contacts cause cell repulsion [26]. Surface N-cad can also regulate other transmembrane receptors, such as the fibroblast growth factor receptor (FGFR) and integrins, on the same cell [16,24,27,28]. Inside the cell, cytoplasmic domain of N-cad binds p120-catenin, β-catenin and α-catenin forming a cadherin-catenin complex (CCC) [29]. The CCC links N-cad to the actin cytoskeleton and regulates signaling, such as inhibiting Rho GTPases through p120-catenin and antagonizing Wnt signaling by competing for β-catenin [30,31]. In addition, the CCC regulates N-cad traffic through the endosomal recycling pathway. Unbound cadherins are rapidly endocytosed and recycled, dependent on p120-catenin [30,32]. N-cad

recycling is important during astrocyte migration to replace surface N-cad at the cell front [33]. Internalized CCCs are also able to signal via Rho GTPases [21,30].

N-cad is upregulated in epithelial cancers during the epithelial-mesenchymal transition and stimulates cell invasion and metastasis [34-36]. Moreover, N-cad expression is upregulated in approximately 60-80% of adult glioblastomas and is associated with increased mortality [37,38]. Inhibiting p120-catenin expression decreases glioma collective invasion in vitro and in vivo [13]. However, over-expression of N-cad inhibits migration and invasion in other glioma models [39,40]. Moreover, N-cad levels are lower in the invasive front than in the tumor mass, suggesting that N-cad interferes with invasion [41]. Thus N-cad may either inhibit or stimulate migration depending on context.

To understand the role of N-cad in pediatric gliomas, we studied PHGGs, which are highly invasive but have different tumor pathologies and rates of malignant progression compared with adult glioblastoma [1]. We found that N-cad inhibits PHGG cell migration on ECM but stimulates migration on neurons or astrocytes, consistent with glioma-glioma cell interactions slowing migration while glioma-neural cell interactions speed migration. PHGG cells leading migration are more dispersed than followers, forming filamentous N-cad junctions with neighboring glioma or normal cells. In contrast, follower cells are tighter packed, forming linear, epithelial-like junctions with their neighbors. The leader cells have higher cell proliferation and nuclear localization of transcription coactivators Yes-associated protein 1 (YAP1) and Transcriptional Coactivator with PDZ-binding motif (TAZ, *WWTR1*), as well as increased N-cad endocytic recycling, when compared with follower cells. YAP1 and TAZ promote internalization and endocytic recycling of N-cad, while N-cad inhibits YAP1 nuclear translocation. Thus, feedback between YAP1/TAZ and N-cad recycling regulates leader-follower phenotypic identity and differential migration on ECM and neural substrates.

Results

N-cad inhibits PHGG migration on ECM but stimulates migration on neural cells.

Pediatric gliomas are thought to arise from neural or glial progenitors [42], which express N-cad as their major cadherin [17,25]. High N-cad expression is associated with poor overall survival in all types of pediatric brain cancer (Figure S1A). N-cad RNA is highly expressed in a set of eight patient-derived PHGG xenografts and cell lines when compared with other cadherins, neuroligin, selectin, nectin, and immunoglobulin superfamily members (NCAM, L1CAM, ALCAM) [43] (Figure S1B and Table S1). N-cad protein was readily detected by Western blotting

in three DMG and two PHGG lines that we analyzed (Figure S1C). These results suggest that N-cad is a widely expressed adhesion protein in pediatric brain tumors and might contribute to disease.

To test if N-cad expression correlates with PHGG invasion and migration, we compared two MYCN-amplified PHGG lines, PBT-04 and PBT-05, which have similar transcript profiles but express lower and higher levels of N-cad respectively (Figures S1B and S1C) [43]. We grew cells as spheroids and measured their migration in different environments. To mimic invasion and migration along the collagen and laminin basement membranes in the perivascular niche [3], spheroids were embedded in Matrigel or incubated on laminin. To mimic invasion into the brain parenchyma and along fiber tracts, spheroids were transferred to aligned primary mouse cerebellar neurons, cultured on nanofibers [44]. We found that lower N-cad-expressing PBT-04 cells invade faster into Matrigel and migrate faster on laminin but migrate slower on neurons, when compared with higher N-cad expressing PBT-05 cells (Figures S1D-S1F).

To test whether high N-cad expression in PBT-05 cells contributes to their slow migration on ECM and fast migration on neurons, we inhibited N-cad expression with shRNA (Figure S1G). N-cad depletion did not affect spheroid formation or cell proliferation rate (Figure S1H-S1J) but increased migration on laminin and invasion into Matrigel (Figures 1A-1D and Video S1) and inhibited migration on aligned cerebellar neurons (Figures 1E-1F). We also measured migration on cultured mouse astrocytes, which mimic the 3D astrocyte-based scaffold in the brain parenchyma [45]. As on neurons, N-cad depletion decreased migration on astrocytes (Figures 1G-1H). This suggests that N-cad levels differentially regulate migration on ECM and on neural or glial cells.

N-cad depletion also increased the number of PBT-05 cells that migrate individually away from the collective, as well as decreasing the number of contacts between cells at the front of the migrating collective (Figures 2A-2C). The remaining connections at the migration front were elongated and may resemble tumor microtubes that connect cells in adult glioblastoma (Figure 2B, arrowhead) [2,8]. These results are consistent with N-cad being the main cell-cell adhesion molecule in this line. N-cad also regulates migration directionality. Analysis of tracks followed by cells during collective migration on laminin or neurons revealed that N-cad depletion increased directionality on laminin but decreased directionality on neurons, without significantly affecting migration speed (Figures 2D-2I). These findings suggest that N-cad regulates the interactions between cells at the leading edge of the collective and has contrary effects on migration

depending on the environment, inhibiting directionality and overall migration and invasion into ECM while stimulating directionality and overall migration into neural and astrocyte environments.

N-cad homotypic interactions slow migration on ECM and speed migration on neurons and astrocytes.

N-cad is known to positively or negatively regulate cell migration through multiple mechanisms, including attracting or repelling cells through homotypic interactions, stimulating other receptors on the same cells, or regulating catenins inside the cells [20,21,24,46]. We wondered whether N-cad homotypic interactions might explain both its positive role in migration over neurons or glia and negative role in migration over ECM. Interactions between glioma cells and normal cells ahead of the collective might increase directionality and stimulate overall migration, while interactions with other glioma cells behind might decrease directionality and inhibit overall migration. This model predicts that N-cad should mediate binding between glioma cells and neurons. To test this, PBT-05 cells were allowed to migrate over cerebellar neurons before fixing and immunostaining for N-cad. Neurons were identified with a transgenic fluorescent reporter and PBT-05 cells by staining with a vital dye. N-cad was detected on both neurons and PBT-05 cells, and localized to filamentous junctions between neurons and PBT-05 cells (Figure 3A and B). To test whether N-cad homotypic interaction is important for migration, we used the $Ncad^{W161A}$ mutant, which inhibits homotypic binding [47,48]. $Ncad^{W161A}$ and $Ncad^{WT}$ were tagged with mCherry and expressed at approximately endogenous level in PBT-05 cells (Figures 3C). As expected, expressing $Ncad^{W161A}$ stimulated single-cell migration and overall collective migration on laminin (Figures 3D-3F), while inhibiting cell migration on neurons (Figures 3G and 3H). Thus homotypic interaction is important for both the positive and negative effects of N-cad on glioma migration. As a further test of whether N-cad in the environment promotes migration, we measured cell migration on a surface coated with the N-cad extracellular domain (ECD). PBT-05 cells migrated rapidly on N-cad ECD, dependent on endogenous N-cad (Figures 3I and 3J). Moreover, PBT-05 cell migration was slower on N-cad-depleted than control astrocytes (Figures 3K-3N). Together, these findings suggest that glioma cell migration is increased or decreased by N-cad homotypic interactions depending on whether the interactions come from ahead of or behind the migrating front (Figure 3O).

Leader and follower cells interconvert during PHGG migration.

Cancer cells leading collective invasion can become specialized and cooperate with follower cells to influence migration speed and directionality [49,50]. Leader cells may be genetically or

epigenetically distinct (predetermined) and become selected to lead migration on the basis of increased migration speed or invasive character, as has been shown in breast and lung cancer [51,52]. Alternatively, leaders and followers may dynamically interchange their places, adapting their phenotype based on their local environment [53-55]. To test whether PBT-05 cells change position during migration, we formed spheroids from cells expressing histone 2B fused to Dendra2, a photoconvertible fluorescent protein. Spheroids were incubated for one day on laminin or neurons or 3 days in Matrigel to allow a migration front to form. Cell nuclei at the migration front were then irradiated to photoconvert Dendra2 from green to red. Migration was then continued for 16 hr (laminin or neurons) or 48 hr (Matrigel, times chosen to allow migration for approximately 27-30 μm under all conditions), and the percent of red cells overtaken by green cells calculated (Figures 4A-4C). Under all migration conditions, ~40-60% of leader cells were overtaken by cells from behind (Figures 4A-4C and Video S2). Thus leader and follower cells interconvert during migration. This suggests that leader cells are not predetermined but dynamically exchange with followers. Leaders may be phenotypically but not genotypically distinct from followers.

Altered N-cad localization and increased N-cad endocytosis in leader cells.

The expression and localization of cadherins is regulated in leader and follower cells during collective migration in development and in invasive carcinoma [46]. Given that N-cad regulates PHGG cell migration, we examined the subcellular localization of N-cad in leaders and followers by immunofluorescence. N-cad localized to epithelial-like junctional complexes between follower cells (yellow arrowheads, Figure 4D r1, orthogonal to line connecting cell nuclei) but was organized along neurite-like cell-cell connections between leader cells (white arrowheads, Figure 4D r2, parallel to line connecting cell nuclei). The leader cell connections may be similar to the filamentous junctions or tumor microtubes formed between infiltrating adult glioblastoma cells at the invasive front [2,13], and resemble those between PBT-05 cells and neurons (Figure 3A). In addition, leader cells contained more N-cad-positive intracellular vesicles than follower cells, suggesting higher N-cad endocytosis (arrow, Figures 4D r2 and 4G). As a control, the number of transferrin receptor-positive endocytic vesicles was the same in leader and follower cells (Figure 4G). N-cad intracellular vesicles colocalized extensively with early endosomes (Rab5), at intermediate levels with recycling endosomes (Rab11), and at low levels with lysosomes (LAMP1) or the Golgi (GM130) (Figures 4E and 4F). These results suggest that N-cad in leader cells forms different types of junctions and may be endocytosed and recycled back to the surface faster than N-cad in follower cells.

To test whether N-cad endocytosis rates differ between leader and follower cells, we quantified N-cad antibody uptake. Migrating PBT-05 cells were cooled to 4 °C and incubated with antibody to the N-cad extracellular domain. Unbound antibody was removed and cells were transferred to 37 °C for different times. Cells were fixed and surface and internalized antibodies were detected using two different fluorescent-conjugated secondary antibodies. Similar amounts of antibody were bound to leader and follower cells initially, but by 20 min twice as much antibody was internalized in leader than follower cells (Figures 4H, 4I and S2A). Internalized N-cad antibodies co-localized extensively with coated vesicles (clathrin) and early endosomes (EEA1 and Rab5), at intermediate levels with recycling endosomes (Rab4 and Rab11), and low level with lysosomes (LAMP1) or the Golgi (GM130) (Figures S2B and S2C). The number of N-cad-positive intracellular vesicles decreased following treatment with clathrin inhibitor Pitstop-2 and dynamin inhibitor Dyngo-4a, which also retarded collective cell migration on laminin (Figure S2D). Together, these findings suggest that N-cad endocytic trafficking is faster in leader than follower cells.

Cadherin endocytosis is regulated in part by p120-catenin binding to the juxtamembrane domain and by cytoskeletal interactions through β- and α-catenin [30]. We wondered if relocalization of N-cad to endosomes in leader cells correlates with altered catenin localization. For this experiment, we engineered PBT-05 cells using CRISPR-Cas9 to express N-cad fused at its C terminus to mGreenLantern (mGL) (Figures 5A-5C). N-cad^{mGL} localized as expected to filamentous junctions (Figure 5D, arrowhead) and intracellular vesicles (Figure 5D, arrows) in leader cells. β-catenin colocalized with N-cad on both the surface and endosomes but p120-catenin was predominantly on the surface (Figure 5D). This is consistent with p120-catenin release during endocytosis, as reported [56]. To test whether N-cad regulates catenin protein levels or localization, we examined control and N-cad-depleted cells (Figures 5E-5H). Western blotting showed that N-cad depletion decreased levels of β- and α-catenin and a mobility shift in p120-catenin (Figure 5E). The mobility shift of p120-catenin may indicate a change in phosphorylation state [30]. Immunofluorescence of mixed cultures of control and N-cad-depleted cells showed that N-cad-depletion decreased both surface and endosomal β- and α-catenin and relocalized p120-catenin from the cell surface to the cytoplasm (Figures 5F-5H). Thus, vesicular traffic of N-cad in leader cells may regulate intracellular signaling by altering the localization of the CCC.

Increased proliferation and YAP1/TAZ signaling in leader cells.

Leader cells from epithelial-derived cancers including breast and lung carcinomas proliferate more slowly than followers [51,53]. To test whether mesenchymal-derived glioma leaders are also less proliferative than followers, we pulse-labeled cells migrating on laminin or neurons or invading Matrigel with EdU [57]. EdU incorporation was significantly higher in leader than follower cells regardless of migration conditions (Figures 6A and 6B; PBT-05 cells were distinguished from neurons using vimentin antibodies). Thus, unlike the situation in breast and lung cancer, PHGG leader cells are more, not less, proliferative than followers.

Leader cells make fewer cell-cell contacts than followers, and cell-cell contacts could regulate proliferation. YAP1 and TAZ (*WWTR1*) are transcriptional coactivators that stimulate cell proliferation, plasticity, and migration during development and disease [58-60]. YAP1/TAZ nuclear localization in epithelial and endothelial cells is inhibited by cell crowding, mediated in part by signals from the CCC [59,61]. PHGG leader cells have fewer cell-cell contacts and altered N-cad subcellular localization, which could induce YAP1 nuclear localization. Indeed, YAP1 immunostaining showed that a higher proportion of leader cells than follower cells had pronounced staining of YAP1 in the nucleus, whether cells were migrating in Matrigel, laminin or neurons (Figures 6C and 6D). Nuclear localization of YAP1 was also higher in leader than follower cells in DMG lines PBT-24 and PBT-29 (Figures S3A and S3B). Thus higher proliferation and higher YAP1/TAZ signaling may specify leader cells during pediatric glioma migration.

Since leader and follower cells change positions during migration, YAP1 subcellular localization may change in parallel. We used PBT-05 cells expressing histone H2B-Dendra2 and photoconverted leader cells after 24 hr of migration. After a further 24 hr of migration, cells were fixed and stained for YAP1. A higher percentage of leader cells had nuclear YAP1 than followers, regardless of whether they had led migration continuously or had recently become leaders (Figure 6E). These results show that YAP1 subcellular distribution changes with cell position during collective migration.

To test whether N-cad regulates YAP1 localization during glioma migration, we analyzed YAP1 distribution in migrating control and N-cad-depleted cells. N-cad depletion increased nuclear YAP1 in leader cells but did not change the low level of nuclear YAP1 in follower cells (Figure 6F). This suggests that nuclear YAP1 increases in leaders if their cell-cell contacts are disrupted by N-cad depletion but remains low in the crowded population of follower cells independent of

N-cad. We tested whether cell crowding regulates YAP1 localization independent of N-cad by plating control or N-cad-depleted cells on a micropatterned coverslip and quantifying nuclear YAP1 in clusters of different sizes (Figures 6G-6H). There was a trend to less nuclear YAP1 as cluster size increased, consistent with larger clusters having more center cells and fewer edge cells, and hence more cell-cell contact, regardless of N-cad status (Figures 6G-6H). The results are consistent with a model in which N-cad regulates glioma cell crowding and the cell density regulates YAP1 localization. The reduced crowding of leader cells may stimulate nuclear translocation of YAP1.

YAP1 stimulates EMT and migration in cancer [58]. We tested whether YAP1 regulates PHGG cell migration. PBT-05 cell migration was significantly inhibited by depleting YAP1 and TAZ with siRNA or by Verteporfin, which inhibits YAP1/TAZ-dependent transcription [62] (Figures 6I-J). Since inhibiting YAP1/TAZ-dependent transcription may inhibit cell proliferation, and cell proliferation may contribute to the migration distance, we also performed spheroid migration assays in basal media without growth factors to minimize cell proliferation. Verteporfin and YAP1/TAZ depletion also inhibited PBT-05 migration in basal media (Figures S3C and S3D). These data suggest that the faster migration of leader cells may be due in part to the lower cell density, decreased N-cad-mediated cell-cell contacts, and consequent increased YAP1/TAZ activity at the migration front.

YAP1/TAZ regulates N-cad endocytosis during PHGG migration.

YAP1/TAZ signaling increases cell-cell junctions and VE-cadherin turnover during vascular development [63,64]. We investigated whether YAP1/TAZ regulates N-cad localization in leader cells. Treatment with YAP1/TAZ siRNAs or Verteporfin did not affect total N-cad expression or N-cad surface levels in leader or follower cells (Figures 7A-7B, S4A-B and S4D). However, YAP1/TAZ knockdown or Verteporfin inhibited N-cad antibody internalization in leader cells, without affecting followers (Figures 7C-7D, S4C and S4E). As a control, transferrin uptake was independent of YAP1/TAZ expression (Figures 7E-7F and S4F). Together, these findings suggest that YAP1/TAZ signaling stimulates N-cad internalization in leader cells, weakening N-cad-mediated cell-cell contacts between leaders and further increasing YAP1 activity through positive feedback. Rapid N-cad endocytosis and recycling in leaders then stimulates their migration relative to followers (Figure 7H).

Discussion

Cancer invasion and metastasis is most efficient when cancer cells adapt their migratory behavior to suit the local microenvironment [12,65]. Our results show that N-cad expression level determines PHGG cell migration efficiency in neural or extracellular matrix environments in vitro. Thus, the level of N-cad might determine the choice of neural or ECM invasion routes in vivo, with higher levels favoring neural or glia invasion and lower levels favoring migration invasion along ECM found around blood vessels and under the pia. In addition, N-cad internalization and recycling are linked to YAP1/TAZ signaling and increased migration speed in a positive feedback loop, such that PHGG leader cells, connected only by filamentous junctions or tumor microtubes, have high rates of N-cad recycling, high YAP1/TAZ signaling, and high proliferation, while follower cells, connected by epithelial-like junctional complexes, are more crowded, have decreased N-cad recycling, low YAP1/TAZ signaling, and low proliferation. These phenotypes of leader and follower cells are not stable and leaders and followers exchange during migration or invasion. Thus, PHGG cells adapt to their surroundings to optimize migration.

Our results show that homotypic N-cad interactions between cells are critical regulators of migration speed. Such interactions could be adhesive. PHGG cells can migrate on an N-cad-coated surface, implying that they can use N-cad homotypic adhesion for force generation. Such forces between PHGG cells might slow migration on ECM but increase migration towards N-cad expressing neurons and astrocytes. However, N-cad interactions are not necessarily adhesive and signaling may also be important. For example, in normal astrocytes or adult glioblastoma cells, N-cad homotypic junctions locally inhibit integrin adhesion, slowing migration and limiting focal adhesions to the leading edge [40]. Similarly, N-cad contacts prevent activation of integrin α5 during somite formation [66]. N-cad-mediated cell-cell contacts also locally inhibit Rac and activate Rho, repressing protrusion and inducing cell polarization and migration away from the point of contact [20,26,67]. Thus, the increased migration of N-cad deficient PHGG cells on ECM may be due to changes in integrin dynamics, the cytoskeleton or cell polarity. Surface N-cad may also regulate PHGG migration through the FGFR. PHGG lines used in our study require FGF for growth, survival and migration. In HEK cells, over-expressed FGFR stabilizes N-cad cell-cell contacts and inhibits migration [27]. On the other hand, N-cad stimulates cortical neuron migration in vivo by stabilizing and activating the FGFR [24]. Therefore, N-cad may regulate PHGG migration on ECM or neurons and glia by a variety of signaling mechanisms involving homotypic interaction.

The stimulation of PHGG migration on neurons and astrocytes by N-cad may also be indirect. We found that N-cad localizes to filamentous junctions between PHGG cells and neurons. These junctions resemble tumor microtubes that provide synaptic contact for neuron to glioma signaling through AMPA-type glutamate receptors in vivo [2,68]. N-cad can regulate AMPA receptor trafficking and activity in neurons [69]. AMPA receptors are abundantly expressed at the invading front and drive glioma invasion [8,70]. In addition, neurons release factors that stimulate glioma proliferation and invasion [71,72]. Thus, N-cad might stimulate PHGG migration over neurons and astrocytes through neuron/glia-specific signaling pathways.

We also found that N-cad endocytosis is regulated during PHGG migration. N-cad but not transferrin endocytosis is increased in leader relative to follower cells although steady-state surface levels are similar. N-cad endocytosis and recycling may promote the migration of PHGG leaders relative to followers. Indeed, N-cad recycling stimulates cortical neuron migration during development [22]. The internalized N-cad co-localizes with β- and α-catenin, suggesting that a functional CCC may be assembled on endosomes. Such internalized CCCs may stimulate directional migration, as has been reported in glial and endothelial cells [21,73]. Inhibiting N-cad internalization in neural crest cells increases cell-cell adhesion, tightly coupling cells together and inhibiting invasion into tight spaces [74]. Also, collective migration and metastasis is more efficient for cancer cells that make weak N-cad cell-cell adhesions (partial EMT) than when cell-cell adhesions are completely disrupted (full EMT) [12,65,75]. Depletion of p120-catenin destabilizes surface N-cad and decreases collective glioblastoma migration [13]. N-cad recycling may thus be important to allow cells to rearrange and cooperate through transient interactions. If cell-cell adhesions are further disrupted, by depleting N-cad or expressing $Ncad^{W161A}$, cells lose their collectiveness and directional migration on neurons and astrocytes. Thus, N-cad endocytosis and recycling enables glioma cells to adapt to their environments, allowing formation of loose filamentous connections between leader cells and tighter junctions between followers.

In addition to N-cad endocytosis, leader cells differed from followers in their increased proliferation and increased nuclear YAP1, regardless of whether they were migrating or invading ECM or neurons. The rapid proliferation of leader cells in PHGG contrasts with the decreased proliferation of leader cells in invasive breast and lung cancer [51,53]. YAP1 and TAZ are transcription factors that stimulate EMT and migration in cancer [58]. YAP1 expression is heterogeneous in glioblastomas, with high YAP1 cells growing faster and becoming clonally dominant [76]. Inhibiting YAP1/TAZ expression or transcription activity in our PHGG cells slowed migration assayed in growth or basal media, suggesting a role for YAP1/TAZ in the faster

migration of leader cells. As nuclear YAP1/TAZ signal was preferentially observed in leader cells in PHGG cells, YAP/TAZ inhibition may result in reduced migratory capacity without substantially reducing tumor bulk culminating in disease control but not eradication.

How are YAP1/TAZ localization, proliferation and N-cad endocytosis linked in leader cells? PHGG leaders and followers switch positions, implying that they are not genetically defined and that cell-extrinsic factors may specify leader and follower phenotypes. Our results suggest a pathway in which decreased crowding of leader cells stimulates YAP1/TAZ nuclear localization and transcription factors to stimulate cell proliferation, cell migration, and N-cad endocytosis. Increased N-cad endocytosis weakens cell-cell junctions in a positive feedback loop and facilitates N-cad recycling to promote migration relative to followers. In support of this model, we found that enforcing cell crowding inhibited YAP1 nuclear localization independent of N-cad; that inhibiting YAP1/TAZ slows cell migration and N-cad endocytosis and stabilizes cell-cell adhesions. A role for YAP1 in stimulating N-cad endocytosis in PHGG cells is consistent with YAP1 regulation of VE-cadherin turnover during vascular development [63].

Overall, we found that N-cad mediates the switch between collective or single-cell migration and allows glioma cells to adapt to their environment. YAP1 and TAZ may respond to cell-cell adhesions and contribute to collective migration plasticity by regulating endocytic trafficking of N-cad in leader cells. While inhibiting N-cad expression would have both beneficial and harmful effects on patients, N-cad recycling might be a therapeutic strategy to inhibit PHGG invasion.

Methods

Cells

Human PHGG cell lines PBT-05 and PBT-04 cells and human DMG cell lines PBT-22, PBT-24 and PBT-29 were a kind gift from James Olson (Seattle Children's Research Institute). PHGG and DMG cells were maintained in glioma growth medium (Human NeuroCult NS-A Proliferation kit (Stemcell Technologies, 05751) supplemented with 20 ng/ml human epidermal growth factor (Invitrogen, PHG0311), 20 ng/ml human basic fibroblast growth factor (Stemcell Technologies, 78003), 2 μg/ml heparin (Stemcell Technologies, 07980), and penicillin-streptomycin (Gibco, 15140-122). Plates were coated with 20 μg/ml laminin (Sigma, L2020) for all lines except PBT-04, which were grown on uncoated plates. Cells were detached with Accutase (Sigma, A6964) for passage. Primary murine astrocytes immortalized with SV40 large T-antigen and H-RasV12 were kindly provided by Amparo Acker-Palmer (Max Planck Institute for Brain Research

Frankfurt) [77]. Murine astrocytes and HEK-293FT cells were maintained in D10 medium (Dulbecco's modified Eagle's medium (Gibco, 11965-092), 10% fetal bovine serum, 2 mM L-glutamine, 1 mM sodium pyruvate, 0.075% sodium bicarbonate and penicillin-streptomycin).

Antibodies

Antibodies	Supplier	Catalog	Dilution
Mouse anti-N-cad (32)	BD Biosciences	610920	Western (1:1000), IF (1:200)
Mouse anti-N-cad (3B9)	Invitrogen	333900	IF (1:200)
Rabbit anti-N-cad (H-63)	Santa Cruz	SC7939	IF (1:200)
Rabbit anti-N-cad	Proteintech	220181AP	Western (1:1000), IF (1:200)
Mouse anti-p120-catenin	BD Biosciences	610133	Western (1:1000), IF (1:200)
Mouse anti-β-catenin	BD Biosciences	610153	Western (1:1000), IF (1:200)
Mouse anti-α-E-catenin	Santa Cruz	SC9988	Western (1:1000), IF (1:200)
Rabbit anti-Vimentin	Abcam	ab19348	IF (1:500)
Mouse anti-Clathrin	BD Biosciences	610499	IF (1:500)
Mouse anti-EEA1	BD Biosciences	610456	IF (1:500)
Mouse anti-Rab5	BD Biosciences	610724	IF (1:500)
Mouse anti-Rab4	BD Biosciences	610888	IF (1:500)
Mouse anti-Rab11	BD Biosciences	610656	IF (1:500)
Goat anti-LAMP1	Santa Cruz	SC8098	IF (1:500)
Mouse anti-GM130	BD Biosciences	610822	IF (1:500)
Mouse anti-YAP1	Abcam	ab56701	Western (1:500), IF (1:200)
Mouse anti-TAZ	BD Biosciences	560235	Western (1:250)
Mouse anti-Vinculin	Sigma	V9131	Western (1:10000)
Mouse anti-β-tubulin	Sigma	T7816	Western (1:10000)
Alexa-Fluor 488 donkey anti-rabbit IgG (H+L)	Invitrogen	A21206	IF (1:500)
Alexa-Fluor 568 goat anti-rabbit IgG (H+L)	Invitrogen	A11011	IF (1:500)
Alexa-Fluor 647 donkey anti-rabbit IgG (H+L)	Invitrogen	A31571	IF (1:500)
Alexa-Fluor 488 goat anti-mouse IgG (H+L)	Invitrogen	A11001	IF (1:500)
Alexa-Fluor 568 goat anti-mouse IgG (H+L)	Invitrogen	A11004	IF (1:500)
Alexa-Fluor 647 goat anti-mouse IgG (H+L)	Invitrogen	A28181	IF (1:500)
Alexa-Fluor 568 donkey anti-goat IgG (H+L)	Invitrogen	A11057	IF (1:500)
IRDye 680RD goat anti-mouse IgG	LI-COR	926-68070	Western (1:5000)

IRDye 800CW goat anti-rabbit IgG	LI-COR	926-32211	Western (1:5000)

DNA constructs and lentiviral transduction

Lentiviral pLKO.1-puromycin negative control and human *CDH2* shRNA vectors were from Sigma-Aldrich

MISSION shRNAs	Catalog no./ Clone ID	Target sequences
pLKO.1-puro non-target shRNA	SHC016	GCGCGATAGCGCTAATAATTT
pLKO.1-puro *CDH2* shRNA #1	TRCN0000312701	GTGCAACAGTATACGTTAATA
pLKO.1-puro *CDH2* shRNA #2	TRCN0000053978	CCAGTGACTATTAAGAGAAAT

pLenti.CAG.H2B.Dendra2.W was a gift from Rusty Lansford (Addgene plasmid #51005; RRID:Addgene_51005). N-cad WT or W161A mutated DNA were amplified by PCR from pCAG-Ncad WT or W161A-HA [24] and cloned into lentiviral pLenti-CAG-mCherry vector using NEBuilder HiFi DNA assembly (New England Biolabs, E2621) to generate pLenti-Ncad WT-HA-mCherry or pLenti-Ncad W161A-HA-mCherry.

To harvest lentiviral particles, lentiviral vector DNA was transfected with psPAX2 and pMD2.G packaging plasmids into HEK-293FT cells using Lipofectamine 2000 transfection reagent (Invitrogen, 11668019) and D10 media lacking antibiotics. After 24 hr, media were changed to glioma growth medium and virus collected for a further 40 hr. Culture media were collected and filtered through a 0.45 μM syringe filter. Glioma cells in a 6-well plate were incubated with 500 μl of viral supernatant and 500 μl growth media for at least 48 hr before selection. pLKO.1-shRNA-puromycin transduced cells were selected with 0.5 μM puromycin for 48 hr. Cells expressing H2B-Dendra2, Ncad WT-HA-mCherry or Ncad W161A-HA-mCherry constructs were sorted on a SONY MA900 Multi-Application Cell Sorter.

Electroporation

For siRNA electroporation, $1X10^6$ cells were mixed with 5 μl of 20 μM siRNAs (GeneSolution siRNA, Qiagen) and 100 μl of Ingenio electroporation solution (Mirus, MIR50114) and nucleofected with an Amaxa Nucleofector I (Lonza) using program C-13 for PHGGs or T-20 for astrocytes. The efficiency of downregulation was validated using western blot.

siRNAs	Catalog no.	Target sequences
Negative control siRNA	1027310	AATTCTCCGAACGTGTCACGT
CDH2 siRNA	1027417	CTGAGCTCAGTTACACTTGAA
Human *YAP1* siRNA 5	1027416	CAGGTGATACTATCAACCAAA
Human *YAP1* siRNA 8		CCGGGATGTCTCAGGAATTGA
Human *YAP1* siRNA 6		CACATCGATCAGACAACAACA

Human *YAP1* siRNA 7		TTGAAGTAGTTTAGTGTTCTA
Human *TAZ (WWTR1)* siRNA 4	1027416	ACAGTAGTACCAAATGCTTTA
Human *TAZ (WWTR1)* siRNA 3		AGACATGAGATCCATCACTAA
Human *TAZ (WWTR1)* siRNA 2		CTGGCTGTAATCACTACCATT
Human *TAZ (WWTR1)* siRNA 1		CTGCGTTCTTGTGACAGATTA

CRISPR-Cas9 knock-in

Single guide RNA (sgRNA) against human *CDH2* (cadherin 2, N-cadherin; gene ID: 1000) intron 15-16 was designed using CHOPCHOP [78]. The sgRNA sequence and its complement with appropriate overhangs, were annealed and cloned at the BbsI site of pORANGE Cloning template vector, a gift from Harold MacGillavry (Addgene plasmid # 131471; http://n2t.net/addgene:131471; RRID: Addgene_131471) [79]. Donor DNA containing a splicing acceptor, *CDH2* exon 16, mGreenLantern without initiation codon and SV40 polyadenylation sequences was assembled using gBlocks HiFi Gene Fragments (Integrated DNA Technologies) and cloned into pORANGE containing the sgRNA using HindIII and XhoI. This single plasmid containing sgRNA, donor DNA and SpCas9 was electroporated into PBT-05 cells and fluorescent cells selected two weeks later using FACS. To confirm the correct insertion, genomic DNA was extracted from fluorescent cells and checked with PCR. Primers for testing insertion; Forward primer 5' TCAGTGATTTTGCCCTTTTGTA 3, Reverse primer 5' GGCTTTCTGATCATCCTGGTAG 3'

	DNA fragment	Sequence (5'-3')
sgRNA	forward	CACCGCGTGCTCTAGCATAGCACAG
	reverse	AAACCTGTGCTATGCTAGAGCACGC
Donor DNA	HindIII+sgRNA	AAGCTTACCACTGTGCTATGCTAGAGCACG
	splicing acceptor	CTAATCTCCTCTCTTCTCCTCTCTCCAG
	CDH2 exon16 + linker	GGCCTTAAAGCGGCTGACAATGACCCCACAGCTCCACCATA TGACTCCCTGTTAGTGTTTGACTATGAAGGCAGTGGCTCCA CTGCTGGGTCCTTGAGCTCCCTTAATTCCTCAAGTAGTGGT GGTGAGCAGGACTATGATTACCTGAACGACTGGGGGCCAC GGTTCAAGAAACTTGCTGACATGTATGGTGGAGGTGATGAC GGCGCTAGC
	mGreenLantern (no ATG) + linker	GTGAGCAAGGGCGAGGAGCTGTTCACCGGGGTGGTGCCCA TCCTGGTCGAGCTGGACGGCGACGTAAACGGCCACAAGTT CAGCGTCCGCGGCGAGGGCGAGGGCGATGCCACCAACGG CAAGCTGACCCTGAAGTTCATCTGCACCACCGGCAAGCTGC CCGTGCCCTGGCCCACCCTCGTGACCACCTTAGGCTACGG CGTGGCCTGCTTCGCCCGCTACCCCGACCACATGAAGCAG CACGACTTCTTCAAGTCCGCCATGCCCGAAGGCTACGTCCA GGAGCGCACCATCTCTTTCAAGGACGACGGTACCTACAAGA CCCGCGCCGAGGTGAAGTTCGAGGGCGACACCCTGGTGAA CCGCATCGTGCTGAAGGGCATCGACTTCAAGGAGGACGGC AACATCCTGGGGCACAAGCTGGAGTACAACTTCAACAGCCA CAAGGTCTATATCACGGCCGACAAGCAGAAGAACGGCATCA AGGCTAACTTCAAGACCCGCCACAACGTTGAGGACGGCGG

		CGTGCAGCTCGCCGACCACTACCAGCAGAACACCCCCATC GGCGACGGCCCCGTGCTGCTGCCCGACAACCACTACCTGA GCCATCAGTCCAAACTGAGCAAAGACCCCAACGAGAAGCGC GATCACATGGTCCTGAAGGAGAGGGTGACCGCCGCCGGGA TTACACATGACATGGACGAGCTGTACAAGTAAAGCGCT
	SV40 poly A	CCATGGCCCAACTTGTTTATTGCAGCTTATAATGGTTACAAA TAAAGCAATAGCATCACAAATTTCACAAATAAAGCATTTTTTT CACTGCATTCTAGTTGTGGTTTGTCCAAACTCATCAATGTAT CTTATCATGTCTGGATCTC
	sgRNA+XhoI	CCACTGTGCTATGCTAGAGCACGCTCGAG

Spheroid migration and invasion

Spheroids were prepared from PBT-05 and PBT-04 cells by seeding $5X10^3$ cells in multiple wells of ultra-low attachment round bottom 96-well plates (Corning, 7007) for 72 hr. Spheroids were prepared similarly from PBT-22, PBT-24 and PBT-29 cells, except the cell number was $2X10^3$ and 0.192% methylcellulose (Sigma, M0512) was included in the media. For migration assays, single spheroids were transferred with 20 μl tips to wells in 48-well plate (Corning, 3548) containing various migration substrates.

To assay migration on ECM, spheroids were transferred to wells that had been coated with 20 μg/ml laminin (PBT-05) or/and 20 μg/ml fibronectin (PBT-04) at 37 °C or with 30 μg/ml of Matrigel (PBT-22, PBT-24 and PBT-29) at 4 °C overnight, drained and washed. Migration was assayed in 200 μl of either a glioma migration medium (Human NeuroCult NS-A Proliferation kit and 20 ng/ml bFGF) or a basal medium (Human NeuroCult NS-A Basal and 20 ng/ml bFGF) were added. Verteporfin was added at 100 nM as needed. Images were taken every 15 minutes for 48 hours on an Incucyte S3 Live-cell analysis system (Sartorius). The area covered by migrating cells was measured with the Incucyte analysis program (Sartorius).

To assay invasion into ECM, spheroids were transferred to wells that had been coated with 30 μg/ml Matrigel (Corning, 356231) then washed. After 1 hr at 37 °C to allow attachment, spheroids were covered with 100 μl 5 mg/ml Matrigel. After an additional 1 hr incubation at 37 °C, 100 μl glioma migration medium was added on top of the Matrigel-embedded spheroids. Phase-contrast images were taken every 24 hours on Nikon Eclipse TS100. The area covered by invading cells was measured with FIJI.

To assay migration on neurons, cerebella were dissected from euthanized wild-type or $Rosa26^{mT/mG}$ (expressing membrane-targeted tandem dimer Tomato) postnatal day 5 mice in dissection solution (1X Hank's balanced salts solution (HBSS, Gibco), 2.5 mM HEPES, 35 mM

glucose, 4 mM sodium bicarbonate and 1.2 mM $MgSO_4$). Isolated brain cerebellar tissues were dissociated with 0.1% trypsin and 0.25 mg/ml deoxyribonuclease I (Sigma, D5319) in dissection solution for 10 min at 37 °C. After tissue fragments had settled, cells were diluted in dissection solution containing deoxyribonuclease I and centrifuged at 200Xg for 5 min. The cell pellet was suspended in granule neuron growth medium (1X Basal medium eagle (Gibco), 10% fetal bovine serum, 1 M KCl and 1X penicillin-streptomycin) and seeded in 0.1 mg/ml poly-D-lysine (Sigma, P0899) pre-coated plates for 20 min at 37 °C to deplete glia. Unattached cells were collected and centrifuged at 200Xg for 5 min, resuspended in growth medium and viable cells counted. $1x10^6$ cells were seeded on 0.5 mg/ml poly-D-lysine-coated sterile 12-mm diameter coverslips or aligned 700nm diameter nanofibers in 24 well plates (Sigma, Z694533). Growth medium was changed on days in vitro (DIV) 1 and 3, adding 10 μg/ml cytosine arabinoside (AraC, Sigma, C6645) to reduce growth of non-neuronal cells. Glioma cells were seeded into 96-well ultra-low attachment round-bottom plates for spheroid production on day 2, including 2.5 μM of CytoTrace Green CMFDA (AAT Bioquest, 22017) in the media to facilitate cell tracking. On the morning and afternoon of DIV5, half of the neuron growth medium was replaced with the glioma migration medium. Glioma cell spheroids were rinsed with the NeuroCult basal medium to wash out remaining CytoTrace Green CMFDA and transferred to the neurons together with 250 μl glioma migration medium. Images were acquired every 24 hours for 3 days on a Zeiss LSM780 confocal microscope. The area covered by migrating cells on neurons was measured with FIJI.

To assay migration on astrocytes, we adapted the 3D astrocyte-derived scaffold procedure described previously [80]. $1X10^5$ immortalized murine astrocytes were cultured on 30 μg/ml Matrigel-coated 12-mm glass coverslips. After 2 days, the culture medium was changed to D10 medium with 5 mM 2-deoxy-D-glucose (Sigma, D8375) and 400 nM rotenone (Sigma, 557368) inhibit metabolism. At day 4, glioma cell spheroids were transferred on top of astrocyte scaffolds with 200 μl glioma migration medium and cultured for 2 days. Cells were fixed with 4% paraformaldehyde (PFA, VWR, 100503-917), for 15 minutes at room temperature (RT) and stained with human-specific anti-vimentin antibodies to visualize glioma cells. Images were acquired on Leica Stellaris 5 (10X/0.40 dry objective). The area covered by migrating cells was quantified with FIJI.

The average cell migration distance for each spheroid was calculated using the formula:

Average cell migration distance =$\sqrt{End\ migration\ area/\pi} - \sqrt{Start\ migration\ area/\pi}$.

Single cell tracking on laminin or neurons

H2B-Dendra2 PBT-05 cell spheroids were formed for 3 days and transferred to laminin or neurons for 6 hr or 24 hr respectively. Migrating leader cells were selectively photoconverted using 405 nm laser (FRAPPA photobleaching module under 5000 ms exposure and 50% laser intensity, Andor iQ3 Mosaic) on an Andor Dragonfly spinning disc confocal microscope equipped with Mosaic (Oxford instrument) and a humidity, CO_2 (5%) and temperature (37 ºC)-controlled chamber. Time-lapse confocal images were collected every 15 min for 16 hr. Nuclear movements of leader and follower cells were tracked over time using Imaris (Oxford instrument) and directionality and velocity of individual cells was quantified using a custom-made open-source computer program, DiPer (ref. [81])

N-cad ECD Fc-guided spheroid migration

A 96-well ELISA high-binding plate (Corning, 9018) was coated with 12.5 μg/ml recombinant human N-cad Fc chimera protein (Asp160-Ala724, R&D systems, 1388-NC) or 20 μg /ml poly-D-lysine in coating buffer (HBSS with 1 mM $CaCl_2$) overnight at 4 °C. Wells were then blocked with 3% BSA in HBSS for 2 hr at RT and washed three times in HBSS supplemented with 1.2 mM $CaCl_2$. Glioma spheroids were transferred to the pre-coated plates and incubated in glioma migration medium for 24 hr at 37 °C, 5% CO_2.

N-cad antibody internalization

Glioma cell spheroids were allowed to migrate on laminin-coated coverslips for 24 hr. Coverslips were transferred to 4 °C and incubated in glioma migration medium containing 10 μg/ml rabbit anti-N-cad antibody (Proteintech, 22018-1-AP), which recognizes the N-cad extracellular domain. After 30 min, cells were washed three times with Human Neurocult NS-A basal medium and then fed with glioma migration medium. Cells were incubated for 0, 10, 20 and 40 min at 37 °C and fixed with 4% PFA for 15 min at RT. We adopted a differential labeling of cell-surface and internalized antibody described in Carrodus et al. [82]. Cells were blocked with 5% BSA in PBS for 30 min at RT and incubated with donkey-anti-rabbit IgG (H+L) Alexa Fluor 647 (1:200), to label the cell-surface bound N-cad antibodies. After 2 hr, remaining rabbit IgG on the surface was blocked with a solution of 0.13 mg/ml AffiniPure Fab fragment goat-anti-rabbit IgG (H+L), 5% BSA in PBS, overnight at 4 °C. After blocking, cells were re-fixed with 4% PFA for 5 minutes at RT, then permeabilized and blocked with 0.1% Triton-X-100, 5% BSA in PBS for 30 minutes

at RT. Another secondary antibody, donkey-anti-rabbit IgG (H+L) Alexa Fluor 488 (1:200), was used to label internalized N-cad antibodies. Additional antibodies were included at this stage to analyze N-cad colocalization with markers of specific subcellular compartments. Confocal images were acquired on Zeiss LSM780 or Leica Stellaris 5 (63X/1.40 oil objective). The number of cell surface or intracellular N-cad antibodies-positive puncta were measured using Imaris (Oxford instrument). The Surface creation tool was used to automatically detect endosomal vesicles. The estimated XY diameter for surface detection was 0.5 μm. Background was subtracted. Colocalization of intracellular N-cad antibodies with other proteins was measured by overlapping volume between 3D surfaces of two proteins.

Transferrin uptake

Unlabeled transferrin was removed by preincubating cells in Human NeuroCult NS-A basal medium for 30 min at 37 °C. Cells were then cooled and incubated with 100 μg/ml Alexa Fluor 568-conjugated transferrin (Sigma, T23365) for 30 min at 4 °C. Cells were washed three times with the basal medium and incubated for 40 min at 37 °C before fixation and imaging.

Western blot

Cells were lysed in ice-cold 1X Triton-X-100 lysis buffer (1% Triton-X-100, 150 mM NaCl, 10 mM HEPES pH7.4, 2 mM EDTA and 50 mM NaF) with additional protease and phosphatase inhibitors (10 μg/ml Aprotinin, 1 mM PMSF and 1 mM sodium vanadate), and insoluble material removed at 14,000Xg for 10 min at 4 °C. Protein concentrations were equalized using a Pierce BCA protein assay kit (Thermo Scientific, 23225), adjusted to 1X SDS sample buffer (50 mM Tris-Cl pH6.8, 2% SDS, 0.1 % bromophenol blue, 10% glycerol), and heated to 95 °C for 5 min. Equal amounts (generally 10-20 μg) of protein were separated by sodium dodecyl sulfate-polyacrylamide gel electrophoresis and transferred to a nitrocellulose membrane. The membrane was blocked in Intercept blocking buffer (LI-COR Biosciences, 927-60003) with 5% BSA for 30 minutes at RT. After blocking, the membrane was probed with primary antibodies overnight at 4 °C, followed by IRDye 680RD goat anti-mouse or 800CW goat anti-rabbit conjugated secondary antibodies for 1 hour at RT. Fluorescent images were detected using the Odyssey Infrared Imaging System (LI-COR Biosciences)

Immunofluorescence

Cells were grown or allowed to migrate on 12-mm diameter coverglasses precoated with an appropriate substrate. Cells were fixed with 4% PFA for 15 min at RT, permeabilized with 0.1% Triton-X-100 in PBS for 10 minutes at RT, and blocked with 5% normal goat serum (Jackson

Immunoresearch, 005-000-121), 2% BSA in PBS for 1 hr at RT. Primary antibodies were diluted in 1% BSA in PBS and incubated overnight at 4 °C. Alexa Fluor-conjugated goat anti-mouse or donkey anti-rabbit IgG (H+L) secondary antibodies were incubated together with Alexa Fluor-conjugated phalloidin (A12380 or A22287) for 1 hr at RT. After 4',6-diamidino-2-phenylindole (DAPI, 1:5000) incubation for 5 minutes at RT, the coverglass was mounted with ProLong Glass Antifade Mount (Invitrogen, P36984). Confocal imaging was performed on a Zeiss LSM780 or a Leica Stellaris 5 confocal microscope.

Cell proliferation

Cells were incubated with 5 μM EdU (5-ethynyl-2´-deoxyuridine) diluted in glioma growth medium for 1 hr (laminin and Matrigel) or 3 hr (neurons) at 37 °C. Cells were fixed with 4% paraformaldehyde for 15 min and permeabilized with 0.5% Triton-X-100 for 20 min at RT. EdU was detected with the Click-it 488 reaction solution (Invitrogen, C10337) for 30 min. Nuclei were stained with Hoechst 33342 for additional 30 min.

Micropattern adhesions

A micropatterned glass coverslip with disc diameters from 10 μm to 100 μm (4dcell.com) was precoated with 20 μg/ml laminin overnight at 37 °C. $1X10^5$ cells were resuspended in 1 ml of glioma migration medium and plated on the laminin-coated micropatterned glass coverslip for 1 hr at 37 °C. Unattached cells were carefully removed and fresh glioma migration medium added. After 48 hours, cells were fixed and stained with YAP1 and N-cad antibodies.

Statistics

The number of replicates for each experiment is described in the figure legends. All experiments were repeated at least three independent biological replicates otherwise noted in the figure legend. Statical analyses were performed using GraphPad Prism 9. *P* values were determined using Unpaired *t*-test, Ordinary one-way ANOVA Holm-Šídák's or Šídák's multiple comparisons test and Two-way ANOVA Šídák's multiple comparisons test.

Graphics

Diagrams were prepared with Biorender.com.

Acknowledgments

We are very grateful to Emily J Girard, Fiona Pakiam and Shelli Morris at Seattle Children's Research Institute for their assistance in providing cells, reagents and technical guidance during this study. We also thank Lena Schroeder, Jin Meng, Peng Guo and Julien Dubrulle in the Cellular Imaging and Bioinformatics Shared Resources at Fred Hutchinson Cancer Center for imaging and analysis assistance, Flow Cytometry core staff for cell sorting instruction and Luna Yu for computational assistance. We thank Saurav Kumar, Amanda Stainer, Liesje Steenkiste, Laura Arguedas-Jimenez, Chris Simpkins, Jay Sarthy, David Helfman and other colleagues for discussions and comments for the manuscript. This research was supported by the Fred Hutch Interdisciplinary training in Cancer Research Program, institutional funds from Fred Hutch and the shared resources of the Fred Hutch/ University of Washington Cancer Consortium (P30 CA015704).

Author contributions

Conceptualization, Methodology, Investigation, Writing – Original Draft, Visualization and Funding acquisition, D.K. and J.A.C.; Resources, J.M.O. and J.A.C.; Supervision, J.M.O. and J.A.C.

Declaration of interests

The authors declare no competing interests.

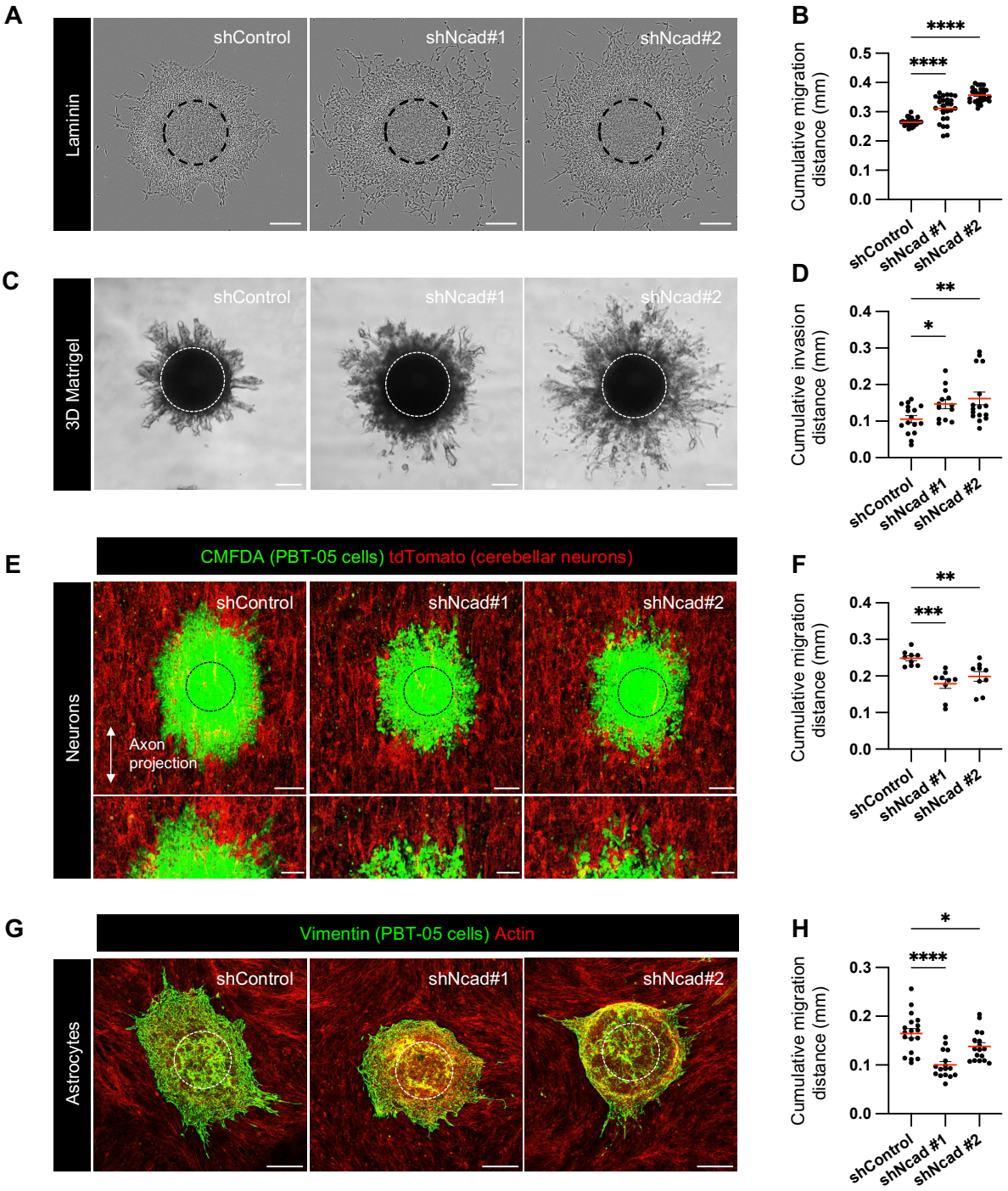

Figure 1 N-cad inhibits PHGG migration on ECMs but stimulate migration on neurons and astrocytes. (A, C) Representative images of migrating control or N-cad shRNA spheroids on laminin for 48 hours or 3D Matrigel for 96 hours. Dashed circles represent spheroid at 0 hours. Scale bars, 200 μm. (B) Cumulative migration distances on laminin for 48 hours. The data represent 27-29 spheroids from 3 independent experiments. (D) Cumulative invasion distances

in 3D Matrigel for 96 hours. The data represent 13-16 spheroids from 4 independent experiments. (E) Cerebellar neurons from Rosa26^{mTmG} postnatal day 5 mice were cultured on the aligned 700nm diameter nanofiber matrix. Neurons expressed tdTomato and PBT-05 were stained with a cell-permeable CMFDA Green fluorescent dye. Scale bars, 200 μm (first row) and 100 μm (second row). (F) Cumulative migration distances on aligned cerebellar neurons for 72 hours. The data represent 9 spheroids from 3 independent experiments. (G) Spheroids migrated in mouse astrocytes for 48 hours. PBT-05 cells were labeled with human-specific anti-vimentin antibodies. Scale bars, 200 μm. (H) Cumulative migration distances were measured after 48 hours of migration in mouse astrocytes. The data represent 16-18 spheroids from 3 independent experiments. The scatter dot plot represents individual spheroids, and the lines indicate mean±s.e.m (B, D, F, H). Ordinary one-way ANOVA Holm-Šídák's multiple comparisons test. *P<0.05, **P<0.01, ***P<0.001, ****P<0.0001.

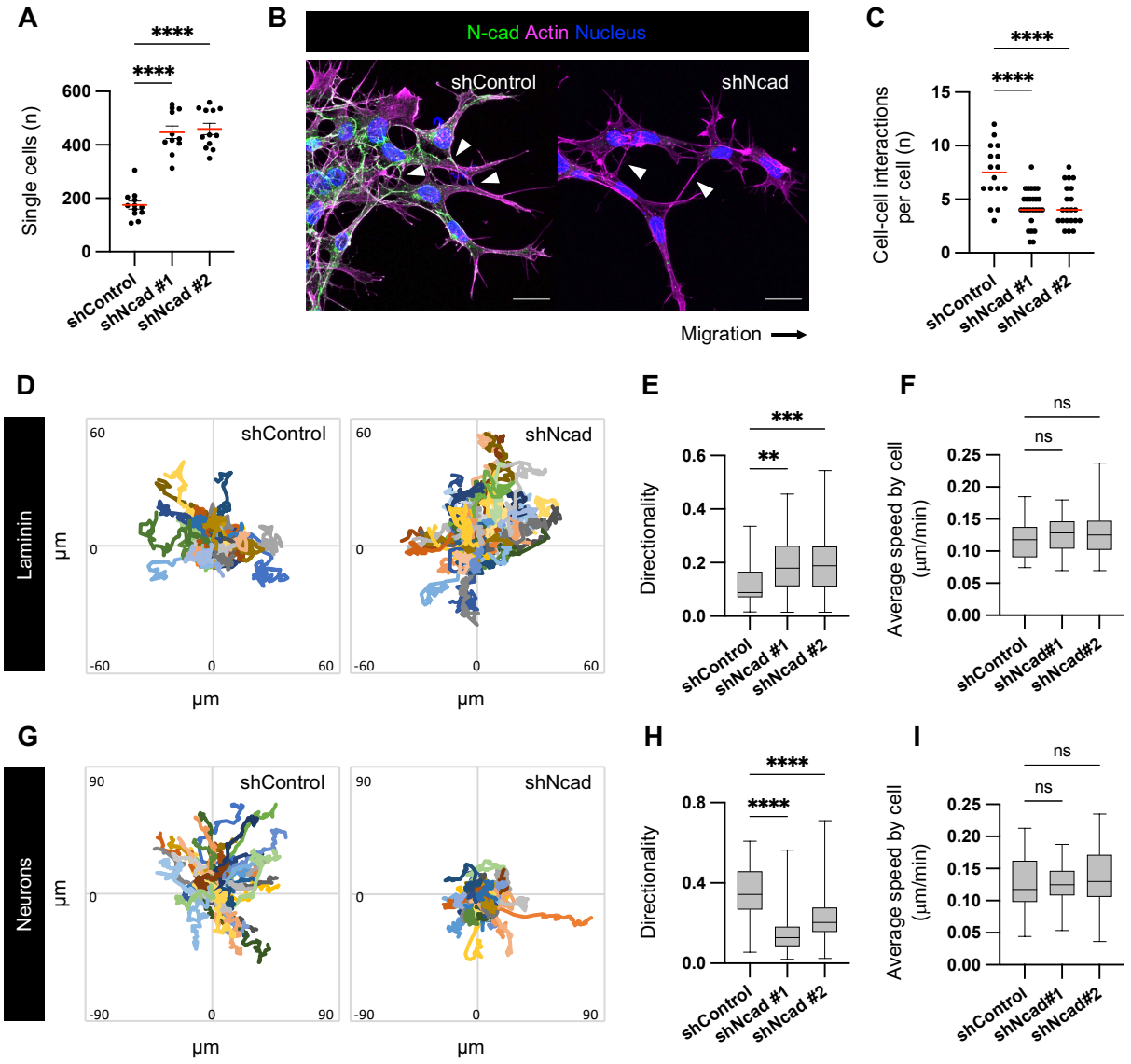

Figure 2 N-cad regulates collective PHGG cell migration. (A) The number of single-cells dissociation from the migration front of the spheroid during 24-hour migration. n=12 spheroids (B-C) The number of cell-cell connections between cells at the leading edge of spheroid cell migration. Scale bar, 20 µm. The data represent 16-26 spheroids from 3 independent experiments. The scatter dot plot represents individual cells, and the lines indicate mean±s.e.m (A, C). (D-I) Cell displacements and directional migration were measured by tracking Dendra2-histone H2B expressing control or N-cad shRNA cells on laminin or neurons for 16 hours. (D-F) In laminin, the data represent 49 cells (shControl), 48 cells (shNcad #1) and 70 cells (shNcad #2) from 3 spheroids. (G-I) In neurons, the data represent 42 cells (shControl), 47 cells (shNcad #1) and 102 cells (shNcad #2) from 3 spheroids. The line within the box plot indicates the

median and the whiskers indicate the min and max (E, F, H, I). Ordinary one-way ANOVA Holm-Šídák's multiple comparisons test. **P<0.01, ***P<0.001, ****P<0.0001.

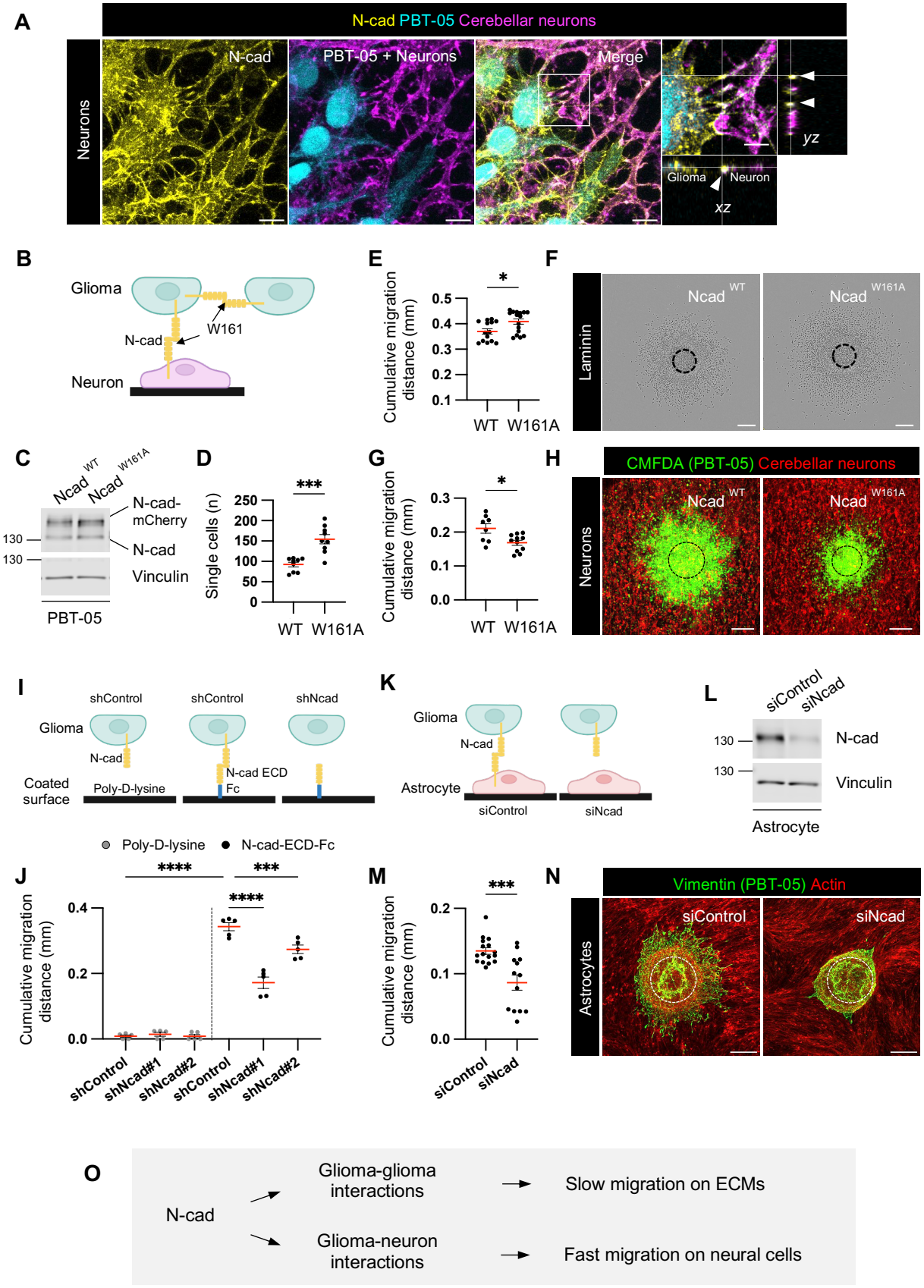
A
N-cad PBT-05 Cerebellar neurons
Neurons
N-cad
PBT-05 + Neurons
Merge
yz
xz
Glioma
Neuron
B
Glioma
N-cad
W161
Neuron
C
Ncad WT
Ncad W161A
N-cad-mCherry
N-cad
Vinculin
130
130
PBT-05
D
Single cells (n)
250
200
150
100
50
0
***
WT W161A
E
Cumulative migration distance (mm)
0.5
0.4
0.3
0.2
0.1
*
WT W161A
F
Laminin
Ncad WT
Ncad W161A
G
Cumulative migration distance (mm)
0.3
0.2
0.1
0.0
*
WT W161A
H
CMFDA (PBT-05) Cerebellar neurons
Neurons
Ncad WT
Ncad W161A
I
shControl
shControl
shNcad
Glioma
N-cad
N-cad ECD
Fc
Coated surface
Poly-D-lysine
K
Glioma
N-cad
Astrocyte
siControl
siNcad
L
siControl
siNcad
130
130
N-cad
Vinculin
Astrocyte
Poly-D-lysine
N-cad-ECD-Fc
J
Cumulative migration distance (mm)
0.4
0.2
0.0
****
***
****
shControl
shNcad#1
shNcad#2
shControl
shNcad#1
shNcad#2
M
Cumulative migration distance (mm)
0.2
0.1
0.0
***
siControl
siNcad
N
Vimentin (PBT-05) Actin
Astrocytes
siControl
siNcad
O
N-cad
Glioma-glioma interactions
Slow migration on ECMs
Glioma-neuron interactions
Fast migration on neural cells

Figure 3 N-cad homotypic interactions slow migration on ECM and speed migration on neurons and astrocytes. (A) PBT-05 spheroid was fluorescently labeled with CMFDA Green and coculture on mouse cerebellar neurons expressing tdTomato for 72 hours. N-cad was stained with the antibody after fixation. The representative image shows the max projection from multiple z-planes. Arrowheads indicate the N-cad localization at cell-cell contacts between PBT-05 cells and neurons. Scale bar, 20 μm and 5 μm (inset). (B) Illustration of N-cad homophilic interactions between glioma cells and between glioma cells and neurons. (C) Western blot analysis for N-cad^{WT}-mCherry or Ncad^{W161A}-mCherry expression in PBT-05 cells. Vinculin is shown as a loading control. (D) The number of single-cells dissociation from the migration front of spheroids after 24 hours of migration on laminin. The data represent 9 spheroids from 3 independent experiments. (E) Cumulative migration distance on laminin for 24 hours. The data represent 14-16 spheroids from 3 independent experiments. (F) Representative images of N-cad^{WT} or Ncad^{W161A} expressing spheroids on laminin after 24 hours of migration on laminin. Scale bars, 200 μm. (G) Cumulative migration distances on neurons for 72 hours. The data represent 8-11 spheroids from 3 independent experiments. (H) Ncad^{WT} and Ncad^{W161A} expressing PBT-05 spheroids were labeled with CMFDA Green and allowed to migrate on aligned cerebellar neurons expressing tdTomato for 72 hours. Scale bars, 200 μm. (I) Spheroids were plated on N-cad extracellular domain (ECD)-Fc coated surface. N-cad ECD provides a substrate for migration and Poly-D-lysin is a negative control. (J) Cumulative migration distances were measured after 24 hours of migration. The data represent 5 spheroids from 2 independent experiments. (K) Illustration of PBT-05 migration on the N-cad depleted astrocyte. (L) Western blots for control or N-cad siRNAs in mouse astrocytes. Vinculin is shown as a loading control. (M) Cumulative migration distances on astrocytes for 48 hours. The data represent 13-16 spheroids from 3 independent experiments. (N) PBT-05 cells migrated on siControl or siNcad-treated mouse astrocytes for 48 hours. Fixed PBT-05 cells were stained with the human-specific vimentin antibody. Scale bars, 200 μm. (O) N-cad-mediated cellular interactions between glioma cells slow migration on ECMs and between glioma cells and neurons speed migration on neurons and astrocytes. The scatter dot plot represents individual cells, and the lines indicate mean±s.e.m (D, E, G, J, M). Unpaired t-test (D, E, G, M). Ordinary one-way ANOVA Šídák's multiple comparisons test (J). *$P<0.05$, ***$P<0.001$, ****$P<0.0001$.

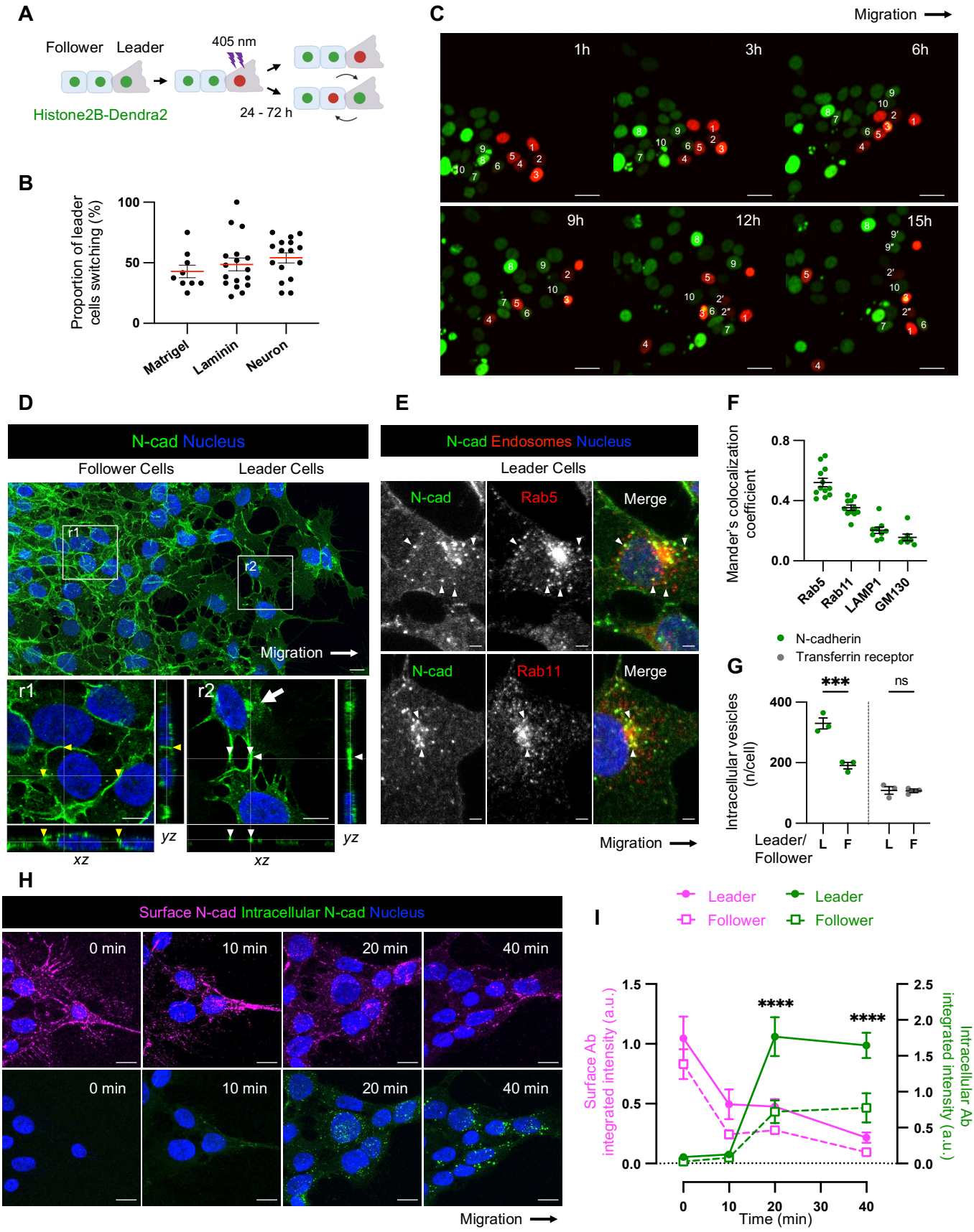
A
Follower
Leader
405 nm
Histone2B-Dendra2
24 - 72 h
B
Proportion of leader cells switching (%)
100
50
0
Matrigel
Laminin
Neuron
C
Migration
1h
3h
6h
9h
12h
15h
D
N-cad Nucleus
Follower Cells
Leader Cells
r1
r2
Migration
yz
xz
E
N-cad Endosomes Nucleus
Leader Cells
N-cad
Rab5
Merge
Rab11
Migration
F
Mander's colocalization coefficient
0.8
0.4
0.0
Rab5
Rab11
LAMP1
GM130
G
N-cadherin
Transferrin receptor
***
ns
Intracellular vesicles (n/cell)
400
200
0
Leader/ Follower
L
F
H
Surface N-cad Intracellular N-cad Nucleus
0 min
10 min
20 min
40 min
Migration
I
Leader
Follower
Surface Ab integrated intensity (a.u.)
Intracellular Ab integrated intensity (a.u.)
1.5
1.0
0.5
0.0
2.5
2.0
1.5
1.0
0.5
0.0
****
****
0
10
20
30
40
Time (min)

Figure 4 Leader and follower cells interconvert during PHGG migration. (A) Schematic diagram of photoconversion of histone H2B-Dendra2 expressing leader cells. (B) The percentage of leader cells switching positions with follower cells in Matrigel, laminin and neurons. After a 72-hour invasion in Matrigel, leader cells were photoconverted green-to-red and incubated additional 48 hours to measure the percentage of leader-follower cell switching during invasion. After 24-hour migration on laminin and neurons, leader cells were highlighted to the red and measured leader and follower cells switching using live-cell imaging for 16 hours. The data represent 9 spheroids (Matrigel), 17 spheroids (laminin) and 16 spheroids (neurons). The scatter plots represent individual spheroids, and the lines indicate mean±s.e.m. (C) Representative still images from a time-lapse movie of histone H2B-Dendra2 spheroid migration on laminin. Nucleus were marked with the red for leader cells and the green for follower cells. Scale bars, 20 μm. (D) Localization of N-cad in leader and follower cells on laminin. The representative immunofluorescent image shows the max projection from multiple z-planes of N-cad and nucleus. Orthogonal views show N-cad localization at the membrane (arrowheads) and perinuclear vesicles (arrows) in follower (r1) and leader (r2) cells. Scale bars, 10 μm or 7 μm (inset). (E) Representative images of migrating cells from spheroids stained for N-cad, Rab5 or Rab11, and nucleus. Arrowheads indicate N-cad-positive endocytic vesicles colocalized with Rab5 or Rab11. Scale bars, 10 μm or 2 μm (inset). (F) Mander's colocalization coefficient was measured by intensity-based colocalization of N-cad with Rab5, Rab11, LAMP1 or GM130. The data represent 7-12 cells from 2-3 spheroids. (G) Intracellular N-cad or transferrin receptor-positive vesicles per cell were measured in leader and follower cells. Each dot represents mean values from 3 independent experiments. Mean±s.e.m. Unpaired t-test. ***$P<0.0001$. ns, not significant. (H) PBT-05 spheroid allowed to migrate on laminin for 24 hours and were incubated with N-cad ECD antibodies at 37 °C for indicated times. Cells were fixed and stained surface or intracellular bound N-cad antibodies with two different fluorescent-conjugated secondary antibodies. Scale bars, 10 μm. (I) Intensity of surface or internalized N-cad Abs were quantified at indicated times. The data represent average values of 7-24 cells from each 2-4 spheroids from 2 independent experiments. Two-way ANOVA Tukey's multiple comparisons test between leader and follower cells at the same time point. ****$P<0.0001$.

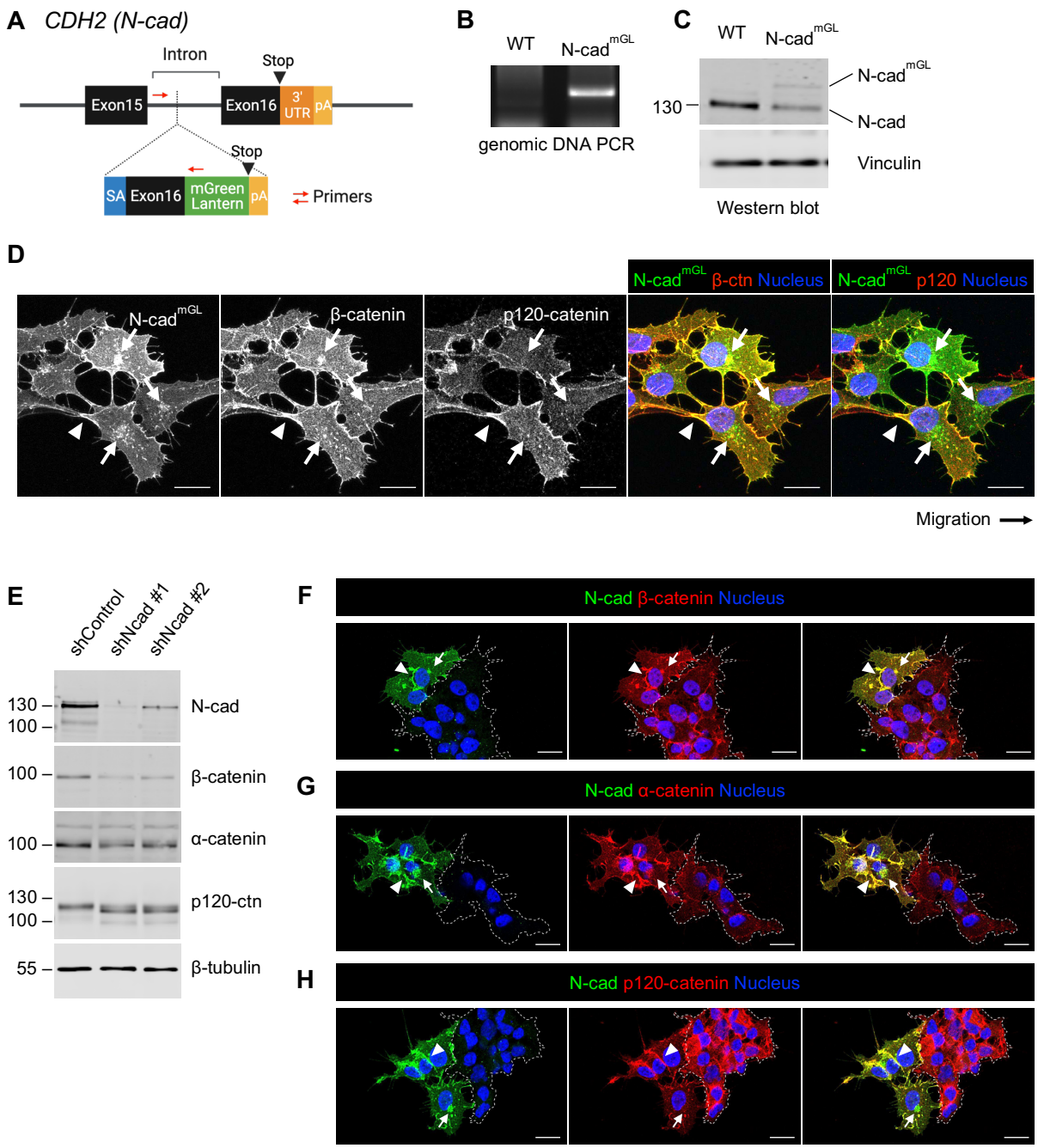

Figure 5 N-cad endocytosis regulates the localization of β-catenin and p120-catenin. (A) Schematic diagram of CRISPR knock-in of mGreenLantern (mGL) at intron 15-16 of human *CDH2* gene. (B) Genomic DNA PCR analysis with the primers shown in (A). (C) Western blot analysis of mGL tagged at the C terminus of N-cad. (D) N-cad^{mGL} were visualized with β-catenin and p120-catenin in leader cells on laminin for 24 hours. Scale bars, 10 μm. (E) Western blot analysis for N-cad, β-catenin, α-catenin, and p120-catenin and β-tubulin is shown as a loading

control. (F-H) Localization of β-catenin, α-catenin and p120-catenin in control or N-cad shRNAs PBT-05 cells. Dashed lines indicate N-cad depleted cells. Arrowheads indicate N-cad at the surface and arrows indicate N-cad intracellular vesicles. Scale bars, 20 μm

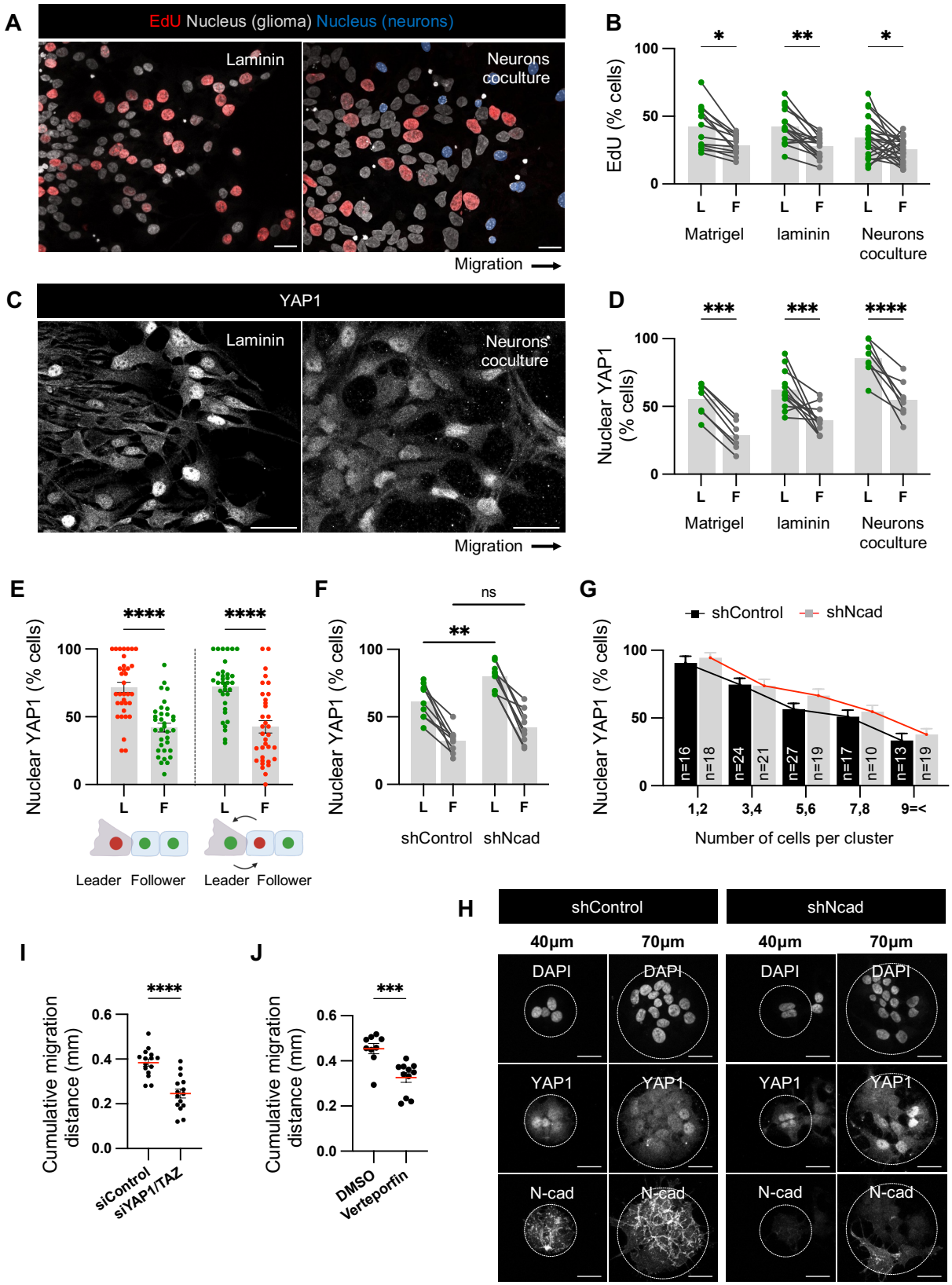
A
EdU Nucleus (glioma) Nucleus (neurons)
Laminin
Neurons coculture
Migration
B
EdU (% cells)
Matrigel
laminin
Neurons coculture
C
YAP1
Laminin
Neurons coculture
Migration
D
Nuclear YAP1 (% cells)
Matrigel
laminin
Neurons coculture
E
Nuclear YAP1 (% cells)
Leader Follower
Leader Follower
F
Nuclear YAP1 (% cells)
ns
shControl shNcad
G
shControl shNcad
Nuclear YAP1 (% cells)
Number of cells per cluster
H
shControl
shNcad
40µm 70µm 40µm 70µm
DAPI
YAP1
N-cad
I
Cumulative migration distance (mm)
siControl siYAP1/TAZ
J
Cumulative migration distance (mm)
DMSO Verteporfin

Figure 6 Increased proliferation and YAP1/TAZ singling in leader cells. (A, C) EdU or YAP1 in leader (L) and follower (F) cells in spheroid cell migration on laminin for 24 hours or neurons for 72 hours. Scale bars, 20 μm. (B, D) Quantification of the percentage of EdU or nuclear YAP1-positive leader and follower cells. PBT-05 spheroids invaded or migrated in Matrigel for 96 hours, laminin for 24 hours and neurons for 72 hours. The data represent 13-23 spheroids from 3-4 independent experiments for EdU and 7-12 spheroids from 3 independent experiments for YAP1. (E) In histone H2B-Dendra2 expressing PBT-05 cells, leader cells were photoconverted to the red after 24-hour of migration on laminin. Percentage of nuclear YAP1 of leader and follower cells were measured additional 24 hours after photoconversion. The data represent 34 spheroids from 3 independent experiments. (F) Quantification of the percentage of nuclear YAP1 of leader and follower cells in control or N-cad shRNA cells. The data represent 9 spheroids from 3 independent experiments. (G) Cells were plated on different sizes of laminin-coated 10-100 μm micropatterned surfaces for 48 hours. The percentage of nuclear YAP1 was measured after staining with YAP1 and nucleus. (H) Representative images of control and N-cad shRNA cells on 40 or 70 μm laminin-coated discs for 48 hours. Scale bar, 20 μm. (I-J) Spheroid cell migration was tested on laminin for 24 hours. DMSO or 0.1 μM Verteporfin was treated when migration begins. The data represent 9-16 spheroids from 3 independent experiments. The bars indicate mean, each dot represents a group of leader or follower cells in the spheroid, and lines between dots indicate cells in the same spheroid (B, D, F). The scatter plots represent individual spheroid, and the lines indicate mean±s.e.m. (E, I, J). Two-way ANOVA Šídák's multiple comparisons test (B, D, F). Ordinary one-way ANOVA Tukey's multiple comparisons test (E). Unpaired t test (I, J). *P<0.05, **P<0.001, ***P<0.001, ****P<0.0001.

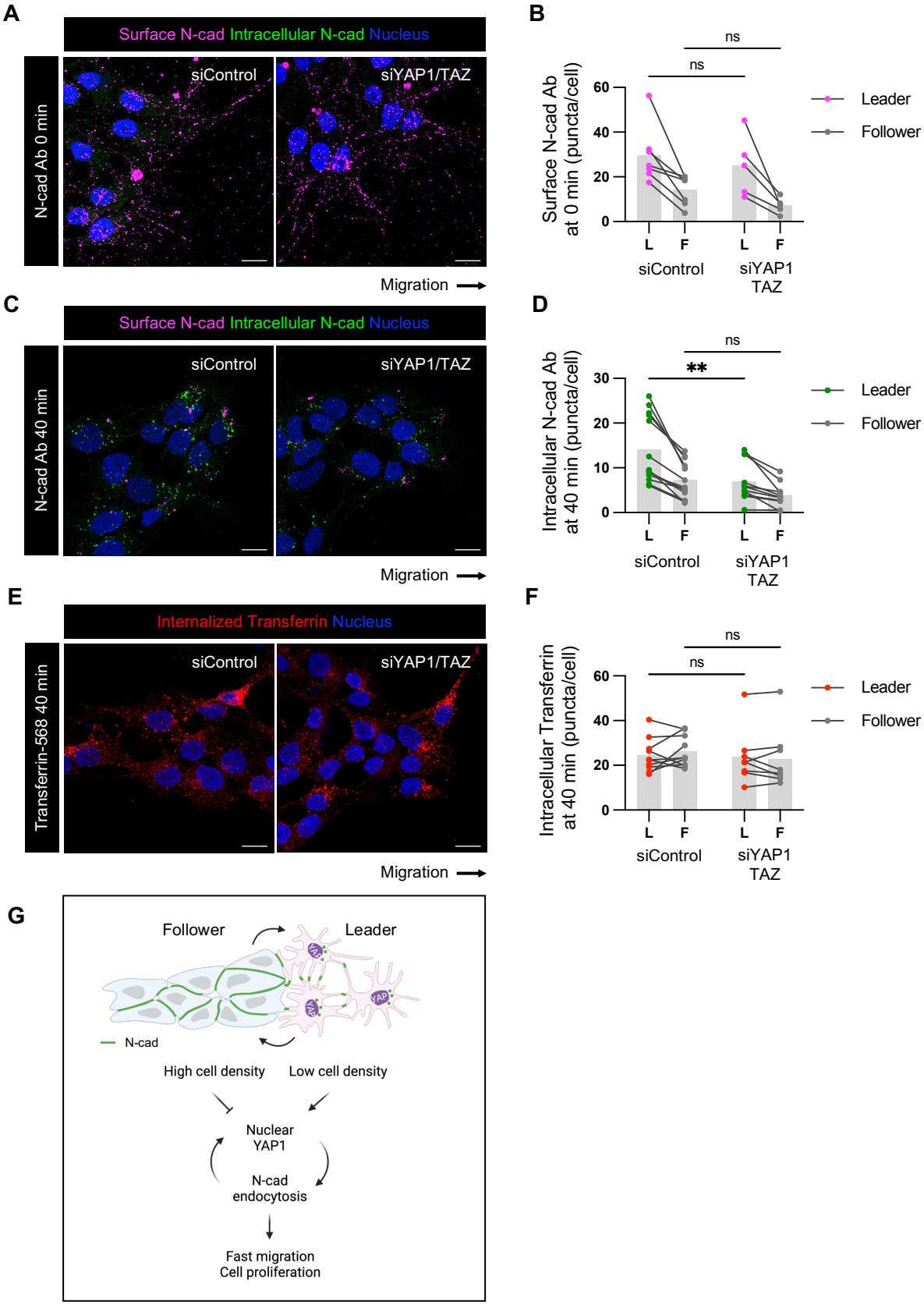
A
Surface N-cad Intracellular N-cad Nucleus
N-cad Ab 0 min
siControl
siYAP1/TAZ
Migration
B
Surface N-cad Ab at 0 min (puncta/cell)
ns
ns
60
40
20
0
L
F
L
F
siControl
siYAP1 TAZ
Leader
Follower
C
Surface N-cad Intracellular N-cad Nucleus
N-cad Ab 40 min
siControl
siYAP1/TAZ
Migration
D
Intracellular N-cad Ab at 40 min (puncta/cell)
ns
**
30
20
10
0
L
F
L
F
siControl
siYAP1 TAZ
Leader
Follower
E
Internalized Transferrin Nucleus
Transferrin-568 40 min
siControl
siYAP1/TAZ
Migration
F
Intracellular Transferrin at 40 min (puncta/cell)
ns
ns
60
40
20
0
L
F
L
F
siControl
siYAP1 TAZ
Leader
Follower
G
Follower
Leader
YAP
N-cad
High cell density
Low cell density
Nuclear YAP1
N-cad endocytosis
Fast migration
Cell proliferation

Figure 7 YAP1/TAZ regulates N-cad endocytosis during PHGG migration. (A, C) Surface N-cad bound Abs were indicated in magenta, internalized N-cad Abs were indicated in green and the nucleus in blue. Scale bars, 10 μm. (B, D) The number of surface localized N-cad Abs (B) or internalized N-cad Abs (D) in migrating leader and follower cells were measured. The data represent 5-13 spheroids from 3 independent experiments. (E-F) The internalization rate of transferrin receptor was analyzed by incubating Alexa Fluor 568-conjugated transferrin for 40 min. The data represent 8-10 spheroids from 3 independent experiments. The bar graphs indicate mean, each dot represents a group of leader or follower cells in the spheroid, and lines between dots indicate cells in the same spheroid (B, D, F). Two-way ANOVA Šídák's multiple comparisons test between leader cells or follower cells in control or YAP1/TAZ siRNAs (B, D, F). ** $P<0.01$. ns, not significant. (G) Phenotypic heterogeneity between leader and follower cells activates YAP1/TAZ and N-cad endocytosis in leader cells and stimulates migration.

References

1. Jones, C., Perryman, L., and Hargrave, D. (2012). Paediatric and adult malignant glioma: close relatives or distant cousins? Nat Rev Clin Oncol *9*, 400-413. 10.1038/nrclinonc.2012.87.
2. Osswald, M., Jung, E., Sahm, F., Solecki, G., Venkataramani, V., Blaes, J., Weil, S., Horstmann, H., Wiestler, B., Syed, M., et al. (2015). Brain tumour cells interconnect to a functional and resistant network. Nature *528*, 93-98. 10.1038/nature16071.
3. Gritsenko, P.G., Ilina, O., and Friedl, P. (2012). Interstitial guidance of cancer invasion. J Pathol *226*, 185-199. 10.1002/path.3031.
4. Cuddapah, V.A., Robel, S., Watkins, S., and Sontheimer, H. (2014). A neurocentric perspective on glioma invasion. Nat Rev Neurosci *15*, 455-465. 10.1038/nrn3765.
5. Neve, A., Santhana Kumar, K., Tripolitsioti, D., Grotzer, M.A., and Baumgartner, M. (2017). Investigation of brain tissue infiltration by medulloblastoma cells in an ex vivo model. Sci Rep *7*, 5297. 10.1038/s41598-017-05573-w.
6. Alieva, M., Leidgens, V., Riemenschneider, M.J., Klein, C.A., Hau, P., and van Rheenen, J. (2019). Intravital imaging of glioma border morphology reveals distinctive cellular dynamics and contribution to tumor cell invasion. Sci Rep *9*, 2054. 10.1038/s41598-019-38625-4.
7. Kluiver, T.A., Alieva, M., van Vuurden, D.G., Wehrens, E.J., and Rios, A.C. (2020). Invaders Exposed: Understanding and Targeting Tumor Cell Invasion in Diffuse Intrinsic Pontine Glioma. Front Oncol *10*, 92. 10.3389/fonc.2020.00092.
8. Venkataramani, V., Yang, Y., Schubert, M.C., Reyhan, E., Tetzlaff, S.K., Wissmann, N., Botz, M., Soyka, S.J., Beretta, C.A., Pramatarov, R.L., et al. (2022). Glioblastoma hijacks neuronal mechanisms for brain invasion. Cell *185*, 2899-2917 e2831. 10.1016/j.cell.2022.06.054.
9. Beadle, C., Assanah, M.C., Monzo, P., Vallee, R., Rosenfeld, S.S., and Canoll, P. (2008). The role of myosin II in glioma invasion of the brain. Mol Biol Cell *19*, 3357-3368. 10.1091/mbc.E08-03-0319.
10. Zarco, N., Norton, E., Quinones-Hinojosa, A., and Guerrero-Cazares, H. (2019). Overlapping migratory mechanisms between neural progenitor cells and brain tumor stem cells. Cell Mol Life Sci *76*, 3553-3570. 10.1007/s00018-019-03149-7.
11. Vinci, M., Burford, A., Molinari, V., Kessler, K., Popov, S., Clarke, M., Taylor, K.R., Pemberton, H.N., Lord, C.J., Gutteridge, A., et al. (2018). Functional diversity and cooperativity between subclonal populations of pediatric glioblastoma and diffuse intrinsic pontine glioma cells. Nat Med *24*, 1204-1215. 10.1038/s41591-018-0086-7.
12. Wu, J.S., Jiang, J., Chen, B.J., Wang, K., Tang, Y.L., and Liang, X.H. (2021). Plasticity of cancer cell invasion: Patterns and mechanisms. Transl Oncol *14*, 100899. 10.1016/j.tranon.2020.100899.
13. Gritsenko, P.G., Atlasy, N., Dieteren, C.E.J., Navis, A.C., Venhuizen, J.H., Veelken, C., Schubert, D., Acker-Palmer, A., Westerman, B.A., Wurdinger, T., et al. (2020). p120-catenin-dependent collective brain infiltration by glioma cell networks. Nat Cell Biol *22*, 97-107. 10.1038/s41556-019-0443-x.
14. Friedl, P., and Mayor, R. (2017). Tuning Collective Cell Migration by Cell-Cell Junction Regulation. Cold Spring Harb Perspect Biol *9*. 10.1101/cshperspect.a029199.
15. Ng, M.R., Besser, A., Danuser, G., and Brugge, J.S. (2012). Substrate stiffness regulates cadherin-dependent collective migration through myosin-II contractility. J Cell Biol *199*, 545-563. 10.1083/jcb.201207148.
16. Collins, C., and Nelson, W.J. (2015). Running with neighbors: coordinating cell migration and cell-cell adhesion. Curr Opin Cell Biol *36*, 62-70. 10.1016/j.ceb.2015.07.004.

17. Hatta, K., and Takeichi, M. (1986). Expression of N-cadherin adhesion molecules associated with early morphogenetic events in chick development. Nature *320*, 447-449. 10.1038/320447a0.
18. Ganzler-Odenthal, S.I., and Redies, C. (1998). Blocking N-cadherin function disrupts the epithelial structure of differentiating neural tissue in the embryonic chicken brain. J Neurosci *18*, 5415-5425. 10.1523/JNEUROSCI.18-14-05415.1998.
19. Xu, X., Li, W.E., Huang, G.Y., Meyer, R., Chen, T., Luo, Y., Thomas, M.P., Radice, G.L., and Lo, C.W. (2001). Modulation of mouse neural crest cell motility by N-cadherin and connexin 43 gap junctions. J Cell Biol *154*, 217-230. 10.1083/jcb.200105047.
20. Theveneau, E., Marchant, L., Kuriyama, S., Gull, M., Moepps, B., Parsons, M., and Mayor, R. (2010). Collective chemotaxis requires contact-dependent cell polarity. Dev Cell *19*, 39-53. 10.1016/j.devcel.2010.06.012.
21. Vassilev, V., Platek, A., Hiver, S., Enomoto, H., and Takeichi, M. (2017). Catenins Steer Cell Migration via Stabilization of Front-Rear Polarity. Dev Cell *43*, 463-479 e465. 10.1016/j.devcel.2017.10.014.
22. Kawauchi, T., Sekine, K., Shikanai, M., Chihama, K., Tomita, K., Kubo, K., Nakajima, K., Nabeshima, Y., and Hoshino, M. (2010). Rab GTPases-dependent endocytic pathways regulate neuronal migration and maturation through N-cadherin trafficking. Neuron *67*, 588-602. 10.1016/j.neuron.2010.07.007.
23. Jossin, Y., and Cooper, J.A. (2011). Reelin, Rap1 and N-cadherin orient the migration of multipolar neurons in the developing neocortex. Nat Neurosci *14*, 697-703. 10.1038/nn.2816.
24. Kon, E., Calvo-Jimenez, E., Cossard, A., Na, Y., Cooper, J.A., and Jossin, Y. (2019). N-cadherin-regulated FGFR ubiquitination and degradation control mammalian neocortical projection neuron migration. Elife *8*. 10.7554/eLife.47673.
25. Kadowaki, M., Nakamura, S., Machon, O., Krauss, S., Radice, G.L., and Takeichi, M. (2007). N-cadherin mediates cortical organization in the mouse brain. Dev Biol *304*, 22-33. 10.1016/j.ydbio.2006.12.014.
26. Scarpa, E., Szabo, A., Bibonne, A., Theveneau, E., Parsons, M., and Mayor, R. (2015). Cadherin Switch during EMT in Neural Crest Cells Leads to Contact Inhibition of Locomotion via Repolarization of Forces. Dev Cell *34*, 421-434. 10.1016/j.devcel.2015.06.012.
27. Nguyen, T., Duchesne, L., Sankara Narayana, G.H.N., Boggetto, N., Fernig, D.D., Uttamrao Murade, C., Ladoux, B., and Mege, R.M. (2019). Enhanced cell-cell contact stability and decreased N-cadherin-mediated migration upon fibroblast growth factor receptor-N-cadherin cross talk. Oncogene *38*, 6283-6300. 10.1038/s41388-019-0875-6.
28. Mui, K.L., Chen, C.S., and Assoian, R.K. (2016). The mechanical regulation of integrin-cadherin crosstalk organizes cells, signaling and forces. J Cell Sci *129*, 1093-1100. 10.1242/jcs.183699.
29. Harris, T.J., and Tepass, U. (2010). Adherens junctions: from molecules to morphogenesis. Nat Rev Mol Cell Biol *11*, 502-514. 10.1038/nrm2927.
30. Reynolds, A.B., and Roczniak-Ferguson, A. (2004). Emerging roles for p120-catenin in cell adhesion and cancer. Oncogene *23*, 7947-7956. 10.1038/sj.onc.1208161.
31. Harris, T.J., and Peifer, M. (2005). Decisions, decisions: beta-catenin chooses between adhesion and transcription. Trends Cell Biol *15*, 234-237. 10.1016/j.tcb.2005.03.002.
32. Le, T.L., Yap, A.S., and Stow, J.L. (1999). Recycling of E-cadherin: a potential mechanism for regulating cadherin dynamics. J Cell Biol *146*, 219-232.
33. Peglion, F., Llense, F., and Etienne-Manneville, S. (2014). Adherens junction treadmilling during collective migration. Nat Cell Biol *16*, 639-651. 10.1038/ncb2985.
34. Mrozik, K.M., Blaschuk, O.W., Cheong, C.M., Zannettino, A.C.W., and Vandyke, K. (2018). N-cadherin in cancer metastasis, its emerging role in haematological

malignancies and potential as a therapeutic target in cancer. BMC Cancer *18*, 939. 10.1186/s12885-018-4845-0.
35. Theveneau, E., and Mayor, R. (2012). Cadherins in collective cell migration of mesenchymal cells. Curr Opin Cell Biol *24*, 677-684. 10.1016/j.ceb.2012.08.002.
36. Noronha, C., Ribeiro, A.S., Taipa, R., Castro, D.S., Reis, J., Faria, C., and Paredes, J. (2021). Cadherin Expression and EMT: A Focus on Gliomas. Biomedicines *9*. 10.3390/biomedicines9101328.
37. Noh, M.G., Oh, S.J., Ahn, E.J., Kim, Y.J., Jung, T.Y., Jung, S., Kim, K.K., Lee, J.H., Lee, K.H., and Moon, K.S. (2017). Prognostic significance of E-cadherin and N-cadherin expression in Gliomas. BMC Cancer *17*, 583. 10.1186/s12885-017-3591-z.
38. Gravendeel, L.A., Kouwenhoven, M.C., Gevaert, O., de Rooi, J.J., Stubbs, A.P., Duijm, J.E., Daemen, A., Bleeker, F.E., Bralten, L.B., Kloosterhof, N.K., et al. (2009). Intrinsic gene expression profiles of gliomas are a better predictor of survival than histology. Cancer Res *69*, 9065-9072. 10.1158/0008-5472.CAN-09-2307.
39. Asano, K., Duntsch, C.D., Zhou, Q., Weimar, J.D., Bordelon, D., Robertson, J.H., and Pourmotabbed, T. (2004). Correlation of N-cadherin expression in high grade gliomas with tissue invasion. J Neurooncol *70*, 3-15. 10.1023/b:neon.0000040811.14908.f2.
40. Camand, E., Peglion, F., Osmani, N., Sanson, M., and Etienne-Manneville, S. (2012). N-cadherin expression level modulates integrin-mediated polarity and strongly impacts on the speed and directionality of glial cell migration. J Cell Sci *125*, 844-857. 10.1242/jcs.087668.
41. Siebzehnrubl, F.A., Silver, D.J., Tugertimur, B., Deleyrolle, L.P., Siebzehnrubl, D., Sarkisian, M.R., Devers, K.G., Yachnis, A.T., Kupper, M.D., Neal, D., et al. (2013). The ZEB1 pathway links glioblastoma initiation, invasion and chemoresistance. EMBO Mol Med *5*, 1196-1212. 10.1002/emmm.201302827.
42. Azzarelli, R., Simons, B.D., and Philpott, A. (2018). The developmental origin of brain tumours: a cellular and molecular framework. Development *145*. 10.1242/dev.162693.
43. Brabetz, S., Leary, S.E.S., Grobner, S.N., Nakamoto, M.W., Seker-Cin, H., Girard, E.J., Cole, B., Strand, A.D., Bloom, K.L., Hovestadt, V., et al. (2018). A biobank of patient-derived pediatric brain tumor models. Nat Med *24*, 1752-1761. 10.1038/s41591-018-0207-3.
44. Fujishima, K., Kurisu, J., Yamada, M., and Kengaku, M. (2020). betaIII spectrin controls the planarity of Purkinje cell dendrites by modulating perpendicular axon-dendrite interactions. Development *147*. 10.1242/dev.194530.
45. Gritsenko, P.G., and Friedl, P. (2018). Adaptive adhesion systems mediate glioma cell invasion in complex environments. J Cell Sci *131*. 10.1242/jcs.216382.
46. Khalil, A.A., and de Rooij, J. (2019). Cadherin mechanotransduction in leader-follower cell specification during collective migration. Exp Cell Res *376*, 86-91. 10.1016/j.yexcr.2019.01.006.
47. Tamura, K., Shan, W.S., Hendrickson, W.A., Colman, D.R., and Shapiro, L. (1998). Structure-function analysis of cell adhesion by neural (N-) cadherin. Neuron *20*, 1153-1163. 10.1016/s0896-6273(00)80496-1.
48. Shapiro, L., Fannon, A.M., Kwong, P.D., Thompson, A., Lehmann, M.S., Grubel, G., Legrand, J.F., Als-Nielsen, J., Colman, D.R., and Hendrickson, W.A. (1995). Structural basis of cell-cell adhesion by cadherins. Nature *374*, 327-337. 10.1038/374327a0.
49. Qin, L., Yang, D., Yi, W., Cao, H., and Xiao, G. (2021). Roles of leader and follower cells in collective cell migration. Mol Biol Cell *32*, 1267-1272. 10.1091/mbc.E20-10-0681.
50. Vilchez Mercedes, S.A., Bocci, F., Levine, H., Onuchic, J.N., Jolly, M.K., and Wong, P.K. (2021). Decoding leader cells in collective cancer invasion. Nat Rev Cancer. 10.1038/s41568-021-00376-8.

51. Konen, J., Summerbell, E., Dwivedi, B., Galior, K., Hou, Y., Rusnak, L., Chen, A., Saltz, J., Zhou, W., Boise, L.H., et al. (2017). Image-guided genomics of phenotypically heterogeneous populations reveals vascular signalling during symbiotic collective cancer invasion. Nat Commun *8*, 15078. 10.1038/ncomms15078.
52. Labernadie, A., Kato, T., Brugues, A., Serra-Picamal, X., Derzsi, S., Arwert, E., Weston, A., Gonzalez-Tarrago, V., Elosegui-Artola, A., Albertazzi, L., et al. (2017). A mechanically active heterotypic E-cadherin/N-cadherin adhesion enables fibroblasts to drive cancer cell invasion. Nat Cell Biol *19*, 224-237. 10.1038/ncb3478.
53. Zhang, J., Goliwas, K.F., Wang, W., Taufalele, P.V., Bordeleau, F., and Reinhart-King, C.A. (2019). Energetic regulation of coordinated leader-follower dynamics during collective invasion of breast cancer cells. Proc Natl Acad Sci U S A *116*, 7867-7872. 10.1073/pnas.1809964116.
54. Nguyen-Ngoc, K.V., Cheung, K.J., Brenot, A., Shamir, E.R., Gray, R.S., Hines, W.C., Yaswen, P., Werb, Z., and Ewald, A.J. (2012). ECM microenvironment regulates collective migration and local dissemination in normal and malignant mammary epithelium. Proc Natl Acad Sci U S A *109*, E2595-2604. 10.1073/pnas.1212834109.
55. Riahi, R., Sun, J., Wang, S., Long, M., Zhang, D.D., and Wong, P.K. (2015). Notch1-Dll4 signalling and mechanical force regulate leader cell formation during collective cell migration. Nat Commun *6*, 6556. 10.1038/ncomms7556.
56. Davis, M.A., Ireton, R.C., and Reynolds, A.B. (2003). A core function for p120-catenin in cadherin turnover. J Cell Biol *163*, 525-534. 10.1083/jcb.200307111.
57. Buck, S.B., Bradford, J., Gee, K.R., Agnew, B.J., Clarke, S.T., and Salic, A. (2008). Detection of S-phase cell cycle progression using 5-ethynyl-2'-deoxyuridine incorporation with click chemistry, an alternative to using 5-bromo-2'-deoxyuridine antibodies. Biotechniques *44*, 927-929. 10.2144/000112812.
58. Zanconato, F., Cordenonsi, M., and Piccolo, S. (2019). YAP and TAZ: a signalling hub of the tumour microenvironment. Nat Rev Cancer *19*, 454-464. 10.1038/s41568-019-0168-y.
59. Panciera, T., Azzolin, L., Cordenonsi, M., and Piccolo, S. (2017). Mechanobiology of YAP and TAZ in physiology and disease. Nat Rev Mol Cell Biol *18*, 758-770. 10.1038/nrm.2017.87.
60. Totaro, A., Panciera, T., and Piccolo, S. (2018). YAP/TAZ upstream signals and downstream responses. Nat Cell Biol *20*, 888-899. 10.1038/s41556-018-0142-z.
61. Kim, N.G., Koh, E., Chen, X., and Gumbiner, B.M. (2011). E-cadherin mediates contact inhibition of proliferation through Hippo signaling-pathway components. Proc Natl Acad Sci U S A *108*, 11930-11935. 10.1073/pnas.1103345108.
62. Liu-Chittenden, Y., Huang, B., Shim, J.S., Chen, Q., Lee, S.J., Anders, R.A., Liu, J.O., and Pan, D. (2012). Genetic and pharmacological disruption of the TEAD-YAP complex suppresses the oncogenic activity of YAP. Genes Dev *26*, 1300-1305. 10.1101/gad.192856.112.
63. Neto, F., Klaus-Bergmann, A., Ong, Y.T., Alt, S., Vion, A.C., Szymborska, A., Carvalho, J.R., Hollfinger, I., Bartels-Klein, E., Franco, C.A., et al. (2018). YAP and TAZ regulate adherens junction dynamics and endothelial cell distribution during vascular development. Elife *7*. 10.7554/eLife.31037.
64. Kim, J., Kim, Y.H., Kim, J., Park, D.Y., Bae, H., Lee, D.H., Kim, K.H., Hong, S.P., Jang, S.P., Kubota, Y., et al. (2017). YAP/TAZ regulates sprouting angiogenesis and vascular barrier maturation. J Clin Invest *127*, 3441-3461. 10.1172/JCI93825.
65. Te Boekhorst, V., and Friedl, P. (2016). Plasticity of Cancer Cell Invasion-Mechanisms and Implications for Therapy. Adv Cancer Res *132*, 209-264. 10.1016/bs.acr.2016.07.005.

66. Julich, D., Cobb, G., Melo, A.M., McMillen, P., Lawton, A.K., Mochrie, S.G., Rhoades, E., and Holley, S.A. (2015). Cross-Scale Integrin Regulation Organizes ECM and Tissue Topology. Dev Cell *34*, 33-44. 10.1016/j.devcel.2015.05.005.
67. Ouyang, M., Lu, S., Kim, T., Chen, C.E., Seong, J., Leckband, D.E., Wang, F., Reynolds, A.B., Schwartz, M.A., and Wang, Y. (2013). N-cadherin regulates spatially polarized signals through distinct p120ctn and beta-catenin-dependent signalling pathways. Nat Commun *4*, 1589. 10.1038/ncomms2560.
68. Venkataramani, V., Tanev, D.I., Strahle, C., Studier-Fischer, A., Fankhauser, L., Kessler, T., Korber, C., Kardorff, M., Ratliff, M., Xie, R., et al. (2019). Glutamatergic synaptic input to glioma cells drives brain tumour progression. Nature *573*, 532-538. 10.1038/s41586-019-1564-x.
69. Nuriya, M., and Huganir, R.L. (2006). Regulation of AMPA receptor trafficking by N-cadherin. J Neurochem *97*, 652-661. 10.1111/j.1471-4159.2006.03740.x.
70. Piao, Y., Lu, L., and de Groot, J. (2009). AMPA receptors promote perivascular glioma invasion via beta1 integrin-dependent adhesion to the extracellular matrix. Neuro Oncol *11*, 260-273. 10.1215/15228517-2008-094.
71. Venkatesh, H.S., Johung, T.B., Caretti, V., Noll, A., Tang, Y., Nagaraja, S., Gibson, E.M., Mount, C.W., Polepalli, J., Mitra, S.S., et al. (2015). Neuronal Activity Promotes Glioma Growth through Neuroligin-3 Secretion. Cell *161*, 803-816. 10.1016/j.cell.2015.04.012.
72. Venkatesh, H.S., Tam, L.T., Woo, P.J., Lennon, J., Nagaraja, S., Gillespie, S.M., Ni, J., Duveau, D.Y., Morris, P.J., Zhao, J.J., et al. (2017). Targeting neuronal activity-regulated neuroligin-3 dependency in high-grade glioma. Nature *549*, 533-537. 10.1038/nature24014.
73. Hayer, A., Shao, L., Chung, M., Joubert, L.M., Yang, H.W., Tsai, F.C., Bisaria, A., Betzig, E., and Meyer, T. (2016). Engulfed cadherin fingers are polarized junctional structures between collectively migrating endothelial cells. Nat Cell Biol *18*, 1311-1323. 10.1038/ncb3438.
74. Kuriyama, S., Theveneau, E., Benedetto, A., Parsons, M., Tanaka, M., Charras, G., Kabla, A., and Mayor, R. (2014). In vivo collective cell migration requires an LPAR2-dependent increase in tissue fluidity. J Cell Biol *206*, 113-127. 10.1083/jcb.201402093.
75. Saxena, K., Jolly, M.K., and Balamurugan, K. (2020). Hypoxia, partial EMT and collective migration: Emerging culprits in metastasis. Transl Oncol *13*, 100845. 10.1016/j.tranon.2020.100845.
76. Liu, Z., Yee, P.P., Wei, Y., Liu, Z., Kawasawa, Y.I., and Li, W. (2019). Differential YAP expression in glioma cells induces cell competition and promotes tumorigenesis. J Cell Sci *132*. 10.1242/jcs.225714.
77. Depner, C., Zum Buttel, H., Bogurcu, N., Cuesta, A.M., Aburto, M.R., Seidel, S., Finkelmeier, F., Foss, F., Hofmann, J., Kaulich, K., et al. (2016). EphrinB2 repression through ZEB2 mediates tumour invasion and anti-angiogenic resistance. Nat Commun *7*, 12329. 10.1038/ncomms12329.
78. Labun, K., Montague, T.G., Krause, M., Torres Cleuren, Y.N., Tjeldnes, H., and Valen, E. (2019). CHOPCHOP v3: expanding the CRISPR web toolbox beyond genome editing. Nucleic Acids Res *47*, W171-W174. 10.1093/nar/gkz365.
79. Willems, J., de Jong, A.P.H., Scheefhals, N., Mertens, E., Catsburg, L.A.E., Poorthuis, R.B., de Winter, F., Verhaagen, J., Meye, F.J., and MacGillavry, H.D. (2020). ORANGE: A CRISPR/Cas9-based genome editing toolbox for epitope tagging of endogenous proteins in neurons. PLoS Biol *18*, e3000665. 10.1371/journal.pbio.3000665.
80. Gritsenko, P., Leenders, W., and Friedl, P. (2017). Recapitulating in vivo-like plasticity of glioma cell invasion along blood vessels and in astrocyte-rich stroma. Histochem Cell Biol *148*, 395-406. 10.1007/s00418-017-1604-2.

81. Gorelik, R., and Gautreau, A. (2014). Quantitative and unbiased analysis of directional persistence in cell migration. Nat Protoc *9*, 1931-1943. 10.1038/nprot.2014.131.
82. Carrodus, N.L., Teng, K.S., Munro, K.M., Kennedy, M.J., and Gunnersen, J.M. (2014). Differential labeling of cell-surface and internalized proteins after antibody feeding of live cultured neurons. J Vis Exp, e51139. 10.3791/51139.